

2021-12

# OC6 Phase Ib: Validation of the CFD predictions of difference-frequency wave excitation on a FOWT semisubmersible

Wang, L

<http://hdl.handle.net/10026.1/18189>

---

10.1016/j.oceaneng.2021.110026

Ocean Engineering

Elsevier BV

---

*All content in PEARL is protected by copyright law. Author manuscripts are made available in accordance with publisher policies. Please cite only the published version using the details provided on the item record or document. In the absence of an open licence (e.g. Creative Commons), permissions for further reuse of content should be sought from the publisher or author.*

# OC6 Phase Ib: Validation of the CFD Predictions of Difference-Frequency Wave Excitation on a FOWT Semisubmersible

Lu Wang<sup>1\*</sup>, Amy Robertson<sup>1</sup>, Jason Jonkman<sup>1</sup>, Yi-Hsiang Yu<sup>1</sup>, Arjen Koop<sup>2</sup>, Adrià Borràs Nadal<sup>3</sup>, Haoran Li<sup>4</sup>, Erin Bachynski-Polić<sup>4</sup>, Romain Pinguet<sup>5,6</sup>, Wei Shi<sup>7</sup>, Xinmeng Zeng<sup>7</sup>, Yang Zhou<sup>8</sup>, Qing Xiao<sup>8</sup>, Rupesh Kumar<sup>9</sup>, Hamid Sarlak<sup>10</sup>, Edward Ransley<sup>11</sup>, Scott Brown<sup>11</sup>, Martyn Hann<sup>11</sup>, Stefan Netzband<sup>12</sup>, Malwin Wermbter<sup>12</sup>, Beatriz Méndez López<sup>13</sup>

<sup>1</sup>National Renewable Energy Laboratory (NREL), Golden, CO, USA

<sup>2</sup>Maritime Research Institute Netherlands (MARIN), Wageningen, Netherlands

<sup>3</sup>IFP Energies nouvelles (IFPEN), Rueil-Malmaison, France

<sup>4</sup>Norwegian University of Science and Technology (NTNU), Trondheim, Norway

<sup>5</sup>Principle Power, Inc. (PPI), Emeryville, CA, USA

<sup>6</sup>Aix-Marseille University, CNRS, Centrale Marseille, Institut de Recherche sur les Phénomènes Hors-Equilibre (IRPHE) UMR 7342, Marseille, France

<sup>7</sup>Dalian University of Technology (DUT), Dalian, China,

<sup>8</sup>University of Strathclyde (UOS), Glasgow, UK

<sup>9</sup>University of Ulsan (UOU), Ulsan, South Korea

<sup>10</sup>Technical University of Denmark (DTU), Kgs. Lyngby, Denmark

<sup>11</sup>University of Plymouth (UOP), Plymouth, UK

<sup>12</sup>Hamburg University of Technology (TUHH), Hamburg, Germany

<sup>13</sup>National Renewable Energy Centre (CENER), Sarriguren (Navarra), Spain

## Abstract

During the previous OC5<sup>1</sup> project, state-of-the-art mid-fidelity engineering tools for floating wind systems were found to consistently underpredict the nonlinear, low-frequency responses of semisubmersible offshore wind platforms, leading to substantial errors in the structural loads because of low-frequency surge and pitch resonance. To examine this underprediction, a coordinated investigation with computational fluid dynamics (CFD) simulations and model-basin experiments was carried out. Both investigations involved a fixed and simplified OC5-DeepCwind semisubmersible in bichromatic waves. The wave excitations—especially the nonlinear, difference-frequency excitation—on the structure from the CFD simulations were compared to the experimental measurements for validation, with uncertainty analyses for both the experimental and the CFD results. Further, the wave excitations on each column of the semisubmersible were measured separately in the experiment, allowing the validation of the CFD results to be done on a per-column basis. Overall, the CFD predictions of the difference-frequency excitations agree with the experimental measurements, suggesting the CFD solutions can be used as a reference for tuning and

\* Corresponding author. E-mail address: Lu.Wang@nrel.gov.

<sup>1</sup> Project under IEA Wind Task 30: Offshore Code Comparison Collaboration, Continued with Correlation (OC5).

improving the engineering-level tools and can provide a means to better understand the underprediction at low frequencies.

**Keywords:** offshore wind; bichromatic wave; CFD; nonlinear excitation; validation; OC6

## 1. Introduction

Compared to fixed-bottom offshore wind turbines, the economics of floating offshore wind turbines (FOWTs) are strongly influenced by the additional costs of the floating substructure, mooring system, and power distribution infrastructure, which account for a significant portion of the capital cost (Maienza et al., 2020). Current designs of the floating substructure for wind turbines are generally inspired by those from the oil and gas industry, which tend to be costly to achieve high safety margins for the permanent residence of personnel and spill prevention. FOWTs, on the other hand, do not have these concerns, and further design optimization and cost reduction are possible by reducing the safety margin (Musial and Butterfield, 2004). To achieve this safely, however, the ability to predict the loads and responses of FOWTs more accurately than current engineering modeling and design tools is critical.

Currently, the predictions of the loading and response of FOWTs, especially during the initial design phase, are mostly done with mid-fidelity engineering-level tools, such as OpenFAST, developed by the National Renewable Energy Laboratory (NREL) (Jonkman, 2013). Compared to higher-fidelity approaches, such as computational fluid dynamics (CFD) simulations, the mid-fidelity tools are computationally more efficient, enabling more comprehensive studies; however, the use of simplified models also leads to critical limitations in the current crop of state-of-the-art engineering-level tools. One such limitation—identified in the recently concluded Offshore Code Comparison Collaboration, Continued with Correlation (OC5) project and in the ongoing OC6 (OC5 with unCertainty) project under the International Energy Agency (IEA) Wind Task 30 framework—is the significant underprediction of the low-frequency, nonlinear wave excitation and the corresponding motion/load responses of semisubmersible FOWTs (Robertson et al., 2017, 2020b).

Semisubmersibles are one of several classes of competitive designs for FOWT substructures (Leimeister et al., 2018). Generally, semisubmersibles have surge and pitch natural frequencies below the typical range of primary wave frequencies to avoid direct wave excitation; however, large surge and pitch motion resonance can still occur because of the small nonlinear, low-frequency wave excitation present in irregular seas (Bayati et al., 2014; Simos et al., 2008, 2018). In the OC5 project, a 10% to 20% underprediction of the ultimate and fatigue loads was observed

with all the engineering models used in the study, and the region with the most severe underprediction was the low-frequency responses (Robertson et al., 2017). This issue has also been encountered by other researchers (Pegalajar-Jurado and Bredmose, 2016; Azcona et al., 2019). To better understand this issue, two experimental campaigns were run in the OC6 project to both reduce the experimental uncertainty in the low-frequency response behavior and to break apart the components of the loading (Robertson et al., 2017, 2020b). Validation with these data sets in Phase Ia of OC6 showed that although the inclusion of full quadratic transfer functions (QTFs) for the wave excitation from second-order potential-flow theory and the addition of Morison drag improved the results, the predicted low-frequency response level did not meet that of the experimental measurements. Further, an apparent conflict in model tuning was observed: models using a large Morison drag coefficient and an added damping matrix tended to provide better predictions of fixed-condition wave excitations and free-decay characteristics compared to models with lower drag coefficients and no added damping but generally produced worse estimations of the floating response at the surge natural frequency (Robertson et al., 2020b).

This initial work in OC6 helped to better confirm and identify the low-frequency hydrodynamic loading problem but did not identify the cause of the persistent underprediction by engineering-level modeling tools. Further investigation is needed to get to the root of the problem; therefore, a new experimental campaign is developed (called OC6 Phase Ib) that, in combination with higher-fidelity models, should provide a better understanding of the physical phenomenon and limitations of the present engineering models. This paper reviews the validation of those high-fidelity models against the new campaign.

The OC6 Phase Ib experimental campaign is developed using a simplified version of the OC5-DeepCwind semisubmersible with the central main column and all cross-members removed; only the three outer columns are kept. This change allows the wave loading on each column of the floater to be measured separately to obtain a better understanding of the effects of the hydrodynamic interactions among the three columns of the semisubmersible. The separate measurements also enable a more detailed comparison with numerical simulations, such as high-fidelity CFD solutions. Finally, the simplified floater geometry reduces the difficulties with meshing for the CFD simulations. The experimental campaign was performed at the Alford Wind-Wave Basin of the Advanced Structures and Composites Center of the University of Maine with the goal of getting more detailed hydrodynamic loading measurements (see Fowler (2021) for a report documenting the experimental setup and procedure). The data

1  
2  
3  
4 from this experimental campaign are accessible from the Data Archive and Portal of the Atmosphere to Electrons  
5  
6 (A2e) research initiative of the U.S. Department of Energy (Robertson, 2021).  
7

8       The focus of this paper is to assess the ability of higher-fidelity CFD tools to accurately predict the low-  
9  
10 frequency hydrodynamic excitation using this data set. A subgroup in OC6 involving various academic and research  
11  
12 institutions and industry partners worldwide modeled the captive semisubmersible using a variety of CFD tools. For  
13  
14 this study, a set of five bichromatic wave conditions were carefully selected (Tom et al., 2019), with each OC6  
15  
16 participant carrying out independent simulations of some or all five wave conditions. The nonlinear, difference-  
17  
18 frequency wave excitations in surge and pitch on the fixed semisubmersible were extracted from the simulation  
19  
20 results. Simulating with bichromatic waves instead of full irregular waves has several advantages. First, the selected  
21  
22 bichromatic waves all have relatively short repeat periods, on the order of 100 seconds full scale, and the CFD  
23  
24 simulations need to run for only a few repeat periods to capture the difference-frequency wave excitation. This leads  
25  
26 to greatly shortened computing time compared to irregular-wave simulations, which typically need to be run for a  
27  
28 three-hour physical time window. Further, the resulting difference-frequency wave excitation from the bichromatic-  
29  
30 wave simulations can be compared directly to the potential-flow QTFs to identify the limitations of second-order  
31  
32 potential-flow theory.  
33

34       Recently, several researchers have also investigated the low-frequency wave excitation and the response of  
35  
36 semisubmersible FOWTs using bichromatic waves. For example, an experimental investigation was documented by  
37  
38 do Carmo et al. (2020), where the measured slow-drift motion was compared to the second-order surge response  
39  
40 amplitude operator obtained from the commercial boundary-element-method software WAMIT (Lee, 1995). The  
41  
42 surge damping coefficients estimated from both free-decay motion and forced oscillation were compared with the  
43  
44 WAMIT computation. Even with the lower damping coefficient from the forced oscillation, the difference-  
45  
46 frequency surge motion was still underpredicted compared to the experiment. It was, therefore, concluded that the  
47  
48 underprediction of the difference-frequency wave excitation must play a role in the observed underprediction of the  
49  
50 floater motion. Lopez-Pavon et al. (2015) performed a captive model experiment with bichromatic incident waves  
51  
52 similar to the present OC6 experimental campaign. Second-order wave excitation from WAMIT was found to  
53  
54 underpredict the difference-frequency wave loads when compared to the measurements, even with full QTFs. The  
55  
56 difference between the experimental and the numerical results widened with the use of Newman's approximation.  
57  
58  
59  
60  
61  
62  
63  
64  
65

1  
2  
3  
4 Different from our prior work on the topic of low-frequency nonlinear hydrodynamics (Robertson et al., 2017,  
5 2018, 2020a, 2020b), which investigated a floating wind semisubmersible in irregular waves with simulations using  
6 mid-fidelity engineering tools based on potential-flow theory and/or Morison equation, the present paper is  
7 concerned with the new experimental campaign with a fixed and simplified floater model in bichromatic waves to  
8 zero in on the nonlinear, difference-frequency wave diffraction loads with validation of high-fidelity CFD  
9 simulations. A formal validation requires an understanding of the uncertainties in both the experimental  
10 measurements and the CFD predictions. On the experimental side, a new approach to estimate the uncertainties of  
11 the various quantities of interest is developed based on past experiences (Robertson et al., 2018, 2020a) and is  
12 documented in this paper. This new approach extends our prior work by introducing formal estimates of  
13 experimental uncertainties from wave reflection and wave contamination in the basin with wave-splitting analyses.  
14 Uncertainty estimations for the CFD solutions are equally important, as demonstrated by recent CFD investigations  
15 of FOWTs by, e.g., Wang et al. (2019), Burmester et al. (2020a, 2020b), and Wang et al. (2021c). The various  
16 sources of CFD uncertainties—including numerical discretization uncertainties, iterative uncertainties, modeling  
17 uncertainties, and statistical uncertainties—in the present bichromatic-wave CFD investigation were already  
18 discussed and estimated whenever possible by Wang et al., (2021a, 2021b); therefore, only a brief overview of the  
19 CFD uncertainties is included in this paper.

20  
21  
22 The CFD results, once validated, provide a valuable approach to tackle the challenge with predicting the  
23 nonlinear, low-frequency wave excitation and structural response. The CFD simulations can be used as references  
24 for tuning the mid-fidelity engineering-level tools in lieu of, or in addition to, the more expensive wave-basin  
25 experiments. Additionally, the CFD simulations enable expedient and nonintrusive extraction of flow-field variables  
26 and flow visualizations, which are critical to obtaining a better understanding of the underprediction issue and  
27 possibly lead to improvements to the model formulation and modeling practices used by the mid-fidelity engineering  
28 design tools.

29  
30 The present paper is organized into the following sections. Section 2 provides an overview of the physical  
31 problem, including the geometry of the adopted semisubmersible floater, the specification of the incident waves, and  
32 the quantities of interest. Sections 3 and 4 provide brief overviews of the experimental and CFD setups, respectively.  
33 Example experimental measurements and CFD predictions along with the postprocessing procedures are  
34 summarized in Section 5. The uncertainties in the experimental measurements and CFD simulations are discussed in

Section 6. Finally, the validation of the CFD solutions with comparison to the experiment is presented in Section 7, followed by comparisons with potential-flow predictions in Section 8. The principal outcomes of the present investigation are summarized in Section 9.

## 2. Problem Description

The focus of this paper is to investigate the wave loads on a fixed FOWT semisubmersible platform fixed in bichromatic incident waves with special attention on the nonlinear, difference-frequency wave excitation. A simplified model of a generic offshore wind platform is derived from the OC5-DeepCwind floater (Robertson et al., 2017) by removing the central main column, the pontoons, and the cross-bracings. This allows us to measure the wave excitation on each column separately, as discussed in Section 3. The geometry of the floater and the adopted coordinate system are shown in Figure 1. The incident waves propagate in the positive  $x$ -direction, and the origin is on the still water level at the center of the calm waterplane area. The resulting model consists of three identical columns forming an equilateral triangle with a center-to-center distance between columns of  $L = 50$  m at full scale. Each column comprises a cylindrical upper column and a heave plate/base column. The upper cylinder has a diameter of 12 m and a draft of 14 m (to the top face of the heave plate), whereas the heave plate has a diameter of 24 m and a height of 6 m, resulting in a total draft of 20 m. All dimensions given here are at full scale; however, all CFD simulations and wave-basin experiments were conducted at a 1:50 model scale.

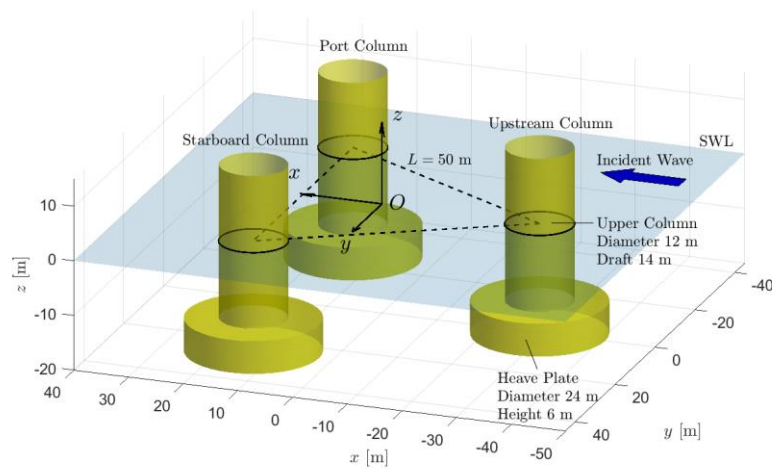


**Figure 1.** Geometry of the FOWT semisubmersible platform and the adopted coordinate system. The still water level (SWL) is indicated by the transparent flat surface. The incident wave is in the positive  $x$ -direction (the blue arrow).

Five different bichromatic wave pairs, named B1 through B5, have been selected for the present analysis (Tom et al., 2019). The properties of the selected waves—including period,  $T_m$ ; frequency,  $f_m$ ; and the prescribed wave amplitude,  $|A_m|$  (magnitude)—are listed in Table 1. The subscript  $m = 1$  or  $2$  is used to denote, respectively, the low-frequency or the high-frequency component of the bichromatic wave pair. The difference frequency,  $f_d$ , between the two wave components and the repeat period,  $T_R$ , are also included. Note that  $T_R$  is also an exact repeat period for the nonlinear frequency components of the bichromatic waves, such as the sum- and difference-frequency components. The wave components are chosen to have relatively short  $T_R$  to reduce the CFD computing time while having  $f_d$  close to the surge or pitch resonance frequency of the OC5-DeepCwind semisubmersible. The waves B1 through B3 all have  $f_d$  near the pitch resonance frequency of 0.032 Hz (Robertson et al., 2020b). B1 and B3 are also chosen to have the same wave frequencies but different wave amplitudes to investigate any amplitude dependence of the difference-frequency wave loads. The waves B4 and B5 have  $f_d$  near the surge resonance frequency of 0.01 Hz (Robertson et al., 2020b). Further, the two wave frequencies of B1, B3, and B5 are close to the peak frequency of the irregular wave spectrum used in prior investigations (Robertson et al., 2020b), whereas B2 and B5 have higher wave frequencies to investigate the frequency dependence.

**Table 1.** Full-scale properties of the selected bichromatic wave pairs.

Wave Case	Wave Period		Frequency		Prescribed Amp.		Diff. Frequency	Repeat Period*
	$T_1$ [s]	$T_2$ [s]	$f_1$ [Hz]	$f_2$ [Hz]	$ A_1 $ [m]	$ A_2 $ [m]	$f_d$ [Hz]	$T_R$ [s]
B1	11.9000	8.6172	0.0840	0.1160	1.76	1.75	0.0320	249.9
B2	9.6000	7.3846	0.1042	0.1354	1.27	1.22	0.0313	96.0
B3	11.9000	8.6172	0.0840	0.1160	1.24	1.30	0.0320	249.9
B4	11.9000	10.5778	0.0840	0.0945	1.75	1.82	0.0105	190.4
B5	9.5345	8.7400	0.1049	0.1144	1.28	1.25	0.0095	104.9

\* The repeat periods are also exact for the nonlinear frequency components, such as the sum/difference-frequency components and higher harmonics.

The primary quantities of interest to be validated are the amplitudes of the wave surge force and pitch moment at the difference frequency. The nonlinear, low-frequency wave excitation, though small, has the potential to excite the surge and pitch resonance frequencies of the floater. The heave force at the difference frequency is less important because the heave natural frequency of the chosen floater design is close to the wave-frequency region, and thus it is excited by the much stronger linear wave excitation. In the present investigation, the amplitudes of the wave excitation in surge and pitch at the difference frequency,  $f_d$ , as well as the two wave frequencies,  $f_1$  and  $f_2$ , are obtained from the wave-load time series by performing fast Fourier transforms (FFTs) over an appropriate time window. The lengths of the time windows are always chosen to be an integer multiple of the bichromatic-wave



repeat periods listed in Table 1. Further, because both the experimental and CFD waves are generally tuned to be within a  $\pm 5\%$  range from the prescribed amplitudes listed in Table 1, it is beneficial to analyze and compare the normalized wave-excitation amplitudes to minimize the impact of the small differences in wave amplitudes.

The complex normalized amplitude of the difference-frequency wave excitation,  $X_j^{(-)}$ , is defined as:

$$X_j^{(-)} = \frac{F_j^{(-)}}{2\rho g L^n A_1^* A_2} \quad (1)$$

where  $F_j^{(-)}$  is the dimensional amplitude of the wave excitation at the difference frequency in surge ( $j = 1$ ) or pitch ( $j = 5$ ). The density of water and the gravitational acceleration are given by  $\rho$  and  $g$ , respectively, and the distance between columns is  $L = 50$  m full scale. The exponent  $n$  is 1 when  $j = 1$  and 2 when  $j = 5$ .  $A_1$  and  $A_2$  are the complex incident wave amplitudes (without the floater) at frequencies  $f_1$  and  $f_2$  at the origin, and  $A_1^*$  is the complex conjugate of  $A_1$ . An additional factor of 2 is included in the denominator to allow for direct comparison with potential-flow QTFs from WAMIT (WAMIT, Inc., 2011), which provide only half of the difference-frequency loads proportional to  $A_1^* A_2$ , not the other half proportional to  $A_1 A_2^*$  (each half is the complex conjugate of the other).

The normalized wave-excitation amplitudes at the two wave frequencies,  $X_{j,m}$ , are defined as:

$$X_{j,m} = \frac{F_{j,m}}{\rho g L^n A_m} \quad (2)$$

where  $F_{j,m}$  is the dimensional amplitude of the wave excitation in mode  $j$  at the wave frequency,  $f_m$ . The exponent  $n$  is 2 when  $j = 1$  and 3 when  $j = 5$ . All other variables are defined in the same fashion as in Eq. (1). The complex wave amplitudes  $A_1$  and  $A_2$  at the two wave frequencies are obtained from the FFTs of the incident wave-elevation time series at the origin from either the wave calibration experiment or the wave-only CFD simulations.

The surge and heave forces are in the directions of the  $x$ -axis and  $z$ -axis, shown in Figure 1, and all pitch moments, including the separate pitch moments on the upstream or starboard column, are always computed about the  $y$ -axis passing through the origin at the center of the calm waterplane area.

### 3. Experimental Setup

An experimental validation campaign as part of OC6 Phase Ib was carried out at the Alford Wind-Wave Basin of the Advanced Structures and Composites Center of the University of Maine. The wave basin, equipped with a 16-paddle wave maker, is 30 m long, 9 m wide; and the depth of the floor was set to 5 m. An elliptical beach opposite

the wave maker is used to dissipate the incident waves. The experimental facility is temperature controlled with minimal fluctuation about the nominal temperature of 18°C, resulting in a freshwater density of 998.6 kg/m<sup>3</sup> with negligible fluctuation.

As shown in Figure 2, the three columns were rigidly and independently mounted to a top-of-column triangular frame, which was fixed to the instrumentation bridge of the wave basin. The upstream and starboard columns were each attached to the triangular frame through a 3-degree-of-freedom load cell, which measured the wave-exciting surge force, heave force, and pitch moment on each column. The separate wave-load measurements allow us to perform more detailed comparisons with the CFD simulations. By port-starboard symmetry, the total wave excitation on the floater is obtained by adding the wave load on the upstream column to twice that on the starboard column.

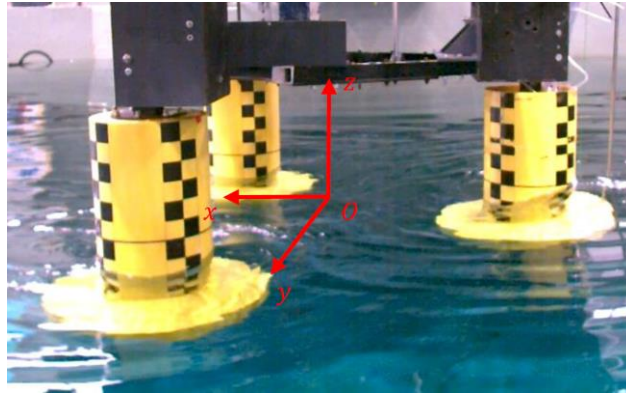


**Figure 2.** Experimental setup of the fixed OC5-DeepCwind semisubmersible without the central main column and cross-members in the Alfond Wind-Wave Basin (photo by the University of Maine).

In addition to the experiments with the floater model, multiple rounds of wave calibration were performed without the structure present to assess the quality and characteristics of the incident waves. During one round of wave calibration, two identical resistance-type wave probes were placed side by side near  $x = 0$ , where the structure would have been centered, at  $y = \pm 0.5$  m basin scale. The two wave probes were taking concurrent measurements. Because the two probes were experiencing mostly the same random fluctuations in the environment, the difference between the measurements from the two wave probes, as discussed in Section 6.1.1, can be used to obtain a measure of the systematic errors in the measured waves. In a separate round of experimental wave calibration, five resistance-type wave probes were placed along the centerline of the wave basin: at  $x = -4.96, -2.49, 0.05, 2.53$ , and  $4.97$  m basin scale, as shown in Figure 3. The measurements from the five probes are used in wave-splitting

analyses to estimate the wave reflections from the downstream beach and to better understand the various wave components at the difference frequency (see Section 6.1.4).

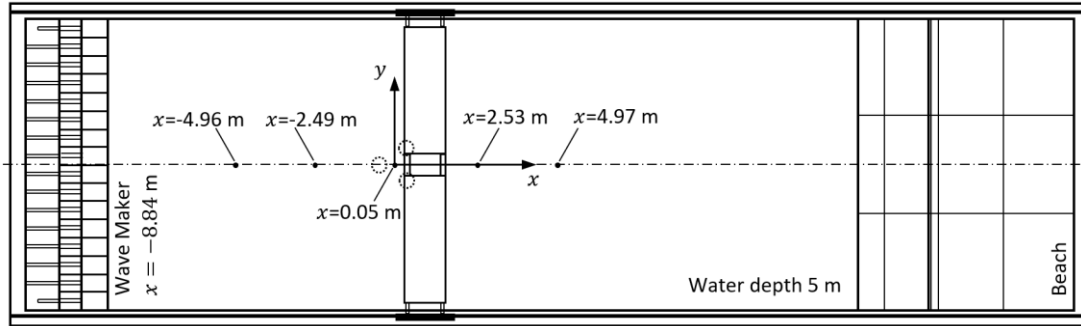


**Figure 3.** Positioning of the three-columned model (three dashed circles near the origin) in the basin and the wave probes (filled dots) along the basin centerline. All dimensions are at the basin scale.

Each experiment used in this paper was repeated three times to enable direct estimates of the random uncertainties without having to assess the individual sources of random errors (Robertson et al., 2020a). Note that the present validation effort uses only a portion of the data collected from the experimental campaign. The full campaign also measured the wave loads on several different model configurations, including two differently sized heave plates, single-column configurations, and configurations where the model has a constant 5-degree pitch offset that mimics the actual operating condition of the FOWT. Further, additional wave conditions, including regular and irregular waves, were also investigated. Finally, the wave runup in front of the upstream column was recorded with an additional wave probe, and the pressure at multiple points on the model surface near the waterline and on the heave plates were measured with pressure transducers. Additional information on the validation campaign is available from Fowler (2021).

## 4. Numerical Setup

For the OC6 Phase Ib CFD investigation, several academic and research institutions and industry partners performed CFD simulations of this experimental campaign. These participants include the National Renewable Energy Centre (CENER) of Spain, the Technical University of Denmark (DTU), Dalian University of Technology (DUT), IFP Energies nouvelles (IFPEN), the Maritime Research Institute Netherlands (MARIN), the National Renewable Energy Laboratory (NREL), the Norwegian University of Science and Technology (NTNU), Principle Power, Inc. (PPI), the University of Plymouth (UOP), the University of Strathclyde (UOS), and the University of

1  
2  
3  
4 Ulsan (UOU). The Hamburg University of Technology (TUHH) also provided results from a time-domain low-order  
5  
6 panel method based on potential-flow theory augmented by Morison drag forces. The initial of each organization in  
7  
8 the parenthesis is used in Section 7 to identify their results.  
9

10 All CFD simulations included here are based on the finite-volume-method solution of the Navier-Stokes  
11  
12 equation and the continuity equation. The CFD software packages used by the participants include ANSYS Fluent  
13  
14 (ANSYS Inc., 2018), OpenFOAM (Weller et al., 1998) with the waves2Foam toolbox (Jacobsen et al., 2012),  
15  
16 ReFresco (ReFresco, 2020), and STAR-CCM+ (Siemens PLM Software, 2018). Both water and air are treated  
17  
18 as viscous and incompressible. The volume-of-fluid formulation (Hirt and Nichols, 1981) was used by all OC6 CFD  
19  
20 participants to model the two-phase free-surface flow problem. We found the standard turbulence models available  
21  
22 to most CFD software packages to be overly dissipative for the present bichromatic-wave problem, resulting in  
23  
24 excessive wave dissipation downstream. (See, e.g., Devolder et al. (2018), Larssen and Fuhrman (2018), and Windt  
25  
26 et al. (2021) for detailed investigations into this issue and possible solutions.) Therefore, all simulations were  
27  
28 performed without any turbulence model (Wang et al., 2021a, 2021b).  
29

30 Further, all CFD simulations were performed at the same 1:50 model scale to be consistent with the wave-basin  
31  
32 experiment for validation purposes. The results shown in this paper have been scaled up to full scale following  
33  
34 Froude scaling. In general, it is difficult to achieve full dynamic similarity with full-scale systems in model-scale  
35  
36 experiments, especially for complex processes; therefore, careful analysis is required to minimize the scaling effects.  
37  
38 The scaling considerations are often specific to the target problem and priorities of the investigation. For example,  
39  
40 see Park et al. (2020) for the scaling of propeller cavitation noise, Canet et al. (2021) on the scaling of wind turbine  
41  
42 rotors, Ueno and Tsukada (2015) on the scaling of ship maneuvering, and Yamini et al. (2018) on the scaling effects  
43  
44 of a porous shore protection structure. The scaling of a FOWT can be particularly challenging because of the  
45  
46 multitude of physical processes and components involved, including turbine aerodynamics, floater hydrodynamics,  
47  
48 structural flexibility, and the mechanical/control system (see, e.g., Martin et al. 2014). To zero in on the nonlinear  
49  
50 hydrodynamic problem, the present investigation is simplified by considering only a fixed structure in waves; thus,  
51  
52 we follow the conventional Froude scaling with both the wave-basin experiment and the CFD simulations. Although  
53  
54 Froude scaling allows the dominant hydrodynamic and gravity effects of a floating offshore wind platform to be  
55  
56 captured (Martin et al. 2014), the low Reynolds number of the model-scale experiment could potentially result in  
57  
58 nonnegligible scaling effects in the nondimensional difference-frequency surge force on the structure for some wave  
59  
60  
61  
62  
63  
64  
65

conditions where the viscous drag force dominates the contributions from higher-order wave diffraction (see Section 8). A quantified analysis of the Reynolds-number scaling effects is beyond the scope of the present investigation, which is focused on the validation of CFD simulations with wave-basin experiments at model scale.

At the start of the OC6 Phase I CFD investigation, a baseline numerical setup was developed and adopted by NREL, which used STAR-CCM+ for the CFD simulations. The details of and the rationale behind the NREL baseline setup were documented by Wang et al. (2021a); therefore, only a brief overview is provided here.

The port-starboard symmetry allows for a half numerical domain, shown in Figure 4, to be used. The Keulegan-Carpenter number based on the diameter of the upper columns is less than 2 for all wave cases (Wang et al., 2021a). Inertial effects dominate (Bocotti, 1996), and we do not expect the formation of asymmetric wakes from flow separation from the columns (Williamson, 1984), which justifies the use of a half domain with symmetry. The model-scale water depth, 5 m, distances from the floater center (origin) to the upstream wave-making boundary, 8.84 m, and to the side boundary, 4.5 m, are all matched exactly between the numerical domain and the physical wave basin. The numerical domain is slightly longer, at 39 m, compared to the physical basin. The longer domain better accommodates a numerical wave damping zone next to the downstream boundary. The length of the damping zone is 8.84 m, which is twice the length of the longest primary linear wave component encountered across all five bichromatic-wave conditions listed in Table 1.

The upstream boundary and bottom boundary are velocity boundaries, where the velocity from the linearized incident wave field is prescribed; however, because of the large water depth, the bottom boundary is basically a no-slip wall. In fact, effectively identical results were obtained with the no-slip condition on the bottom (Wang et al., 2021a). The top and downstream boundaries are pressure outlets, where the hydrostatic pressure is prescribed along with extrapolated backflow directions. The side boundary and the center plane are both symmetry planes. The surface of the structure is a no-slip wall.

The baseline grid consists of 6 million cells for the half domain. The mesh in the vicinity of the free surface and the structure is refined. The mesh-refinement zones and target cell sizes were documented by Wang et al. (2021a). The time step depends on the incident waves and is always set to  $T_2/1030$ , where  $T_2$  is the period of the shorter wave component of each bichromatic wave pair in Table 1. The temporal and spatial discretization schemes are all formally second order, and pressure-velocity coupling is achieved with the Semi-Implicit Method for Pressure Linked Equations (SIMPLE) with 40 iterations per time step. The High-Resolution Interface-Capturing scheme is

used for the advection of the phase volume fraction to maintain a sharp water-air interface. The Courant number near the free surface is kept at less than 0.3, satisfying the Courant number requirement of less than 0.5, stipulated in the STAR-CCM+ documentation (Siemens PLM Software, 2018).

The baseline setup was shared with the OC6 CFD participants at the beginning of the project. Based on experience, software capabilities, and computing resources, the participants developed their own CFD setup with varying degrees of modification to the baseline configuration. Some of the changes include using different numerical schemes, having different domain sizes, using a downstream wave relaxation zone instead of damping zone and an upstream wave-forcing zone, having a nonreflective Sommerfeld boundary condition, generating waves based on second-order bichromatic-wave solution instead of linear superposition, having a free-slip condition on the floater instead of no-slip, and simulating with a full domain instead of a half domain. Selected aspects of the participant CFD setups are documented in the appendix.

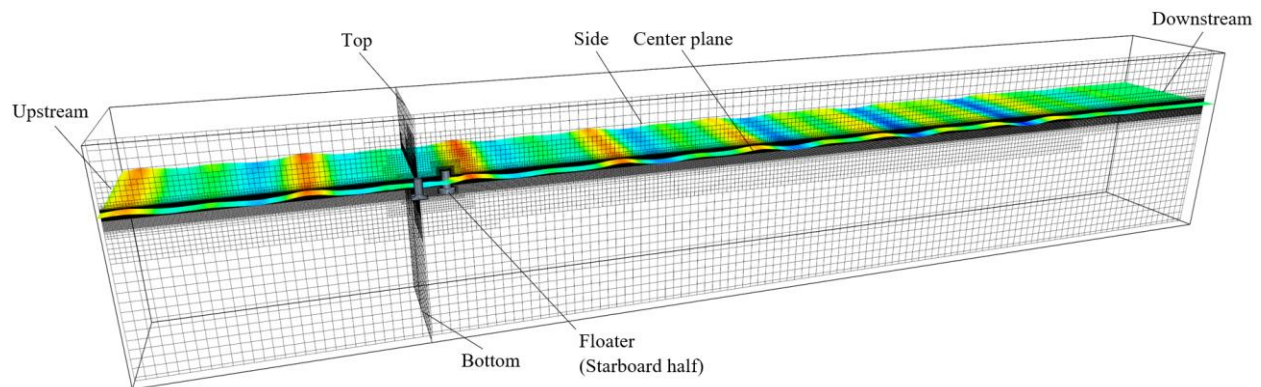


**Figure 4.** The half numerical domain and computational grid of the baseline CFD setup.

## 5. Example CFD and Experimental Results

As an example, the experimentally measured time series of the surge force, heave force, and pitch moment (scaled to full scale with Froude scaling using a full-scale saltwater density of  $1025 \text{ kg/m}^3$ ) on the upstream and starboard columns with Wave B1 are shown in Figure 5. The corresponding results from the CFD simulation performed by NREL are also included for comparison. The experimental and the CFD time series are visually in good agreement. Further, the three repeats of the experiment yield nearly identical time histories visually, indicating good repeatability.

By performing an FFT analysis on the wave-load time series over a suitable time window, the complex amplitudes of the wave excitation at frequencies of interest can be extracted. Time windows of lengths equal to integer multiples of the bichromatic-wave repeat periods toward the end of the runs are used for this purpose. As an example, the amplitude spectra of the time series shown in Figure 5a are shown in Figure 6. With the use of bichromatic waves, the wave-load signals contain only discrete frequency components at the two primary wave frequencies and other higher-order components at zero frequency, sum/difference frequencies, and higher harmonic frequencies. The load components at the difference frequency,  $f_d$ , and the two primary wave frequencies,  $f_1$  and  $f_2$ , are marked by blue circles. The amplitudes (magnitudes) of these frequency components, after normalization following Eq. (1) and Eq. (2), are used as metrics for the validation of the CFD simulations.

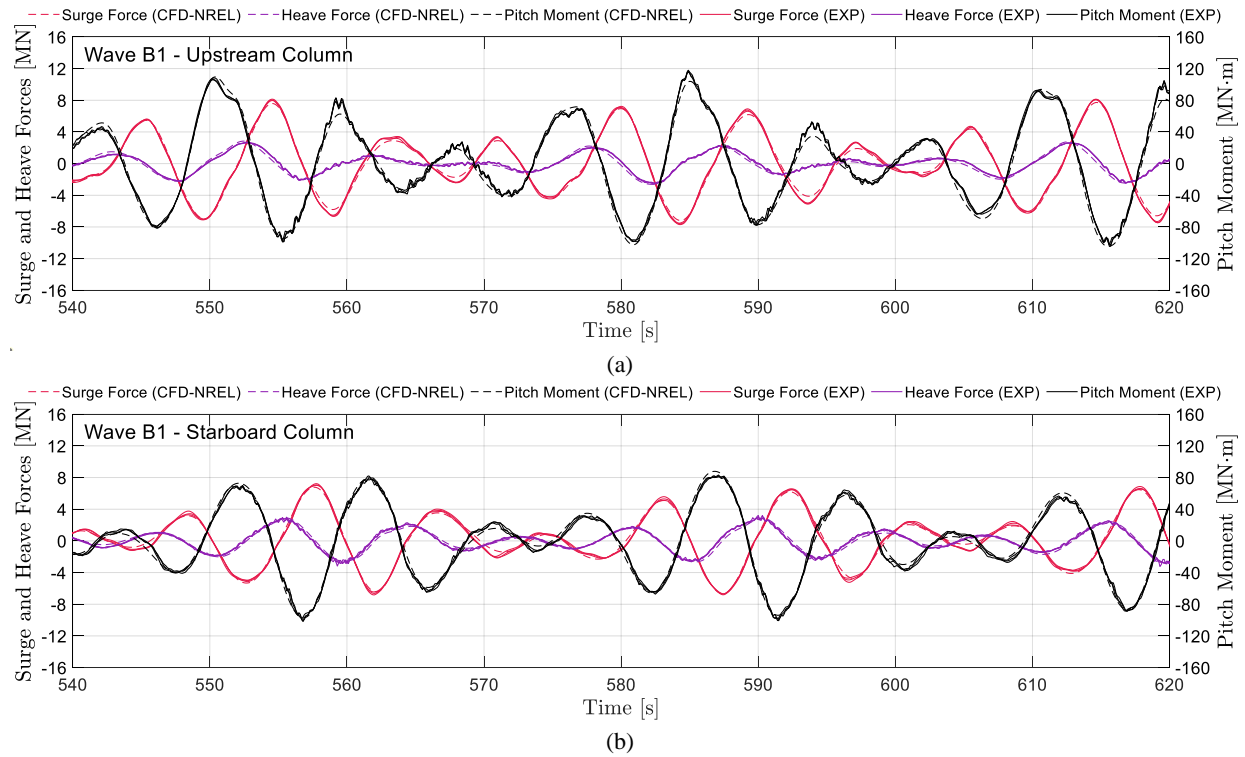


**Figure 5.** Full-scale surge force, heave force, and pitch moment on (a) the upstream column and (b) the starboard column in Wave B1. The time series from the NREL CFD simulation (CFD-NREL) have been shifted in time to align with the experimental measurements (EXP). The experimental measurements from the three repeats are shown together using the same line style and color.

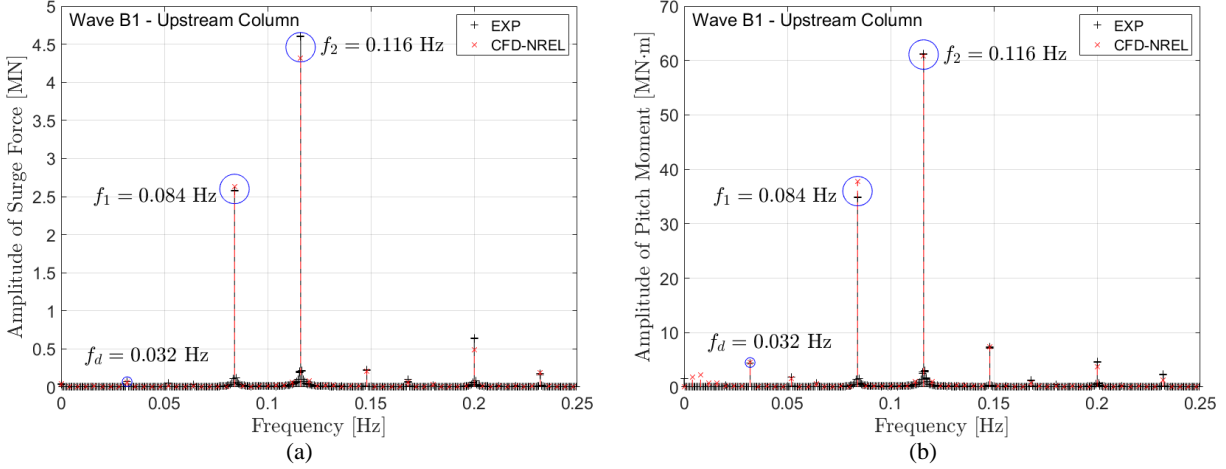


**Figure 6.** The amplitude spectra of the full-scale wave-exciting (a) surge force and (b) pitch moment on the upstream column in Wave B1. Results from the three repeats of the experiment (EXP) are shown together with the results from the corresponding CFD simulation performed by NREL (CFD-NREL).

## 6. Estimation of Experimental and Numerical Uncertainties

A formal validation of the CFD predictions requires uncertainty estimates for both the experimental and numerical results. In Section 6.1, we focus on the estimation of the experimental uncertainties of the various quantities of interest. The uncertainties of the CFD results of the present problem were investigated in prior studies (Wang et al., 2021a, 2021b), and only a brief overview is included in Section 6.2.

### 6.1. Errors and uncertainties of the experimental results

In this section, the various sources of uncertainty in the measured waves and wave excitations are discussed, and the overall approach toward obtaining the uncertainty estimates needed for validating the CFD solutions is outlined. The uncertainties in the measured wave amplitudes and wave-excitation amplitudes are considered first in Section 6.1.1 and Section 6.1.2, respectively, and combined in Section 6.1.3. The systematic errors caused by the small wave reflection from the elliptical beach and the presence of spurious linear waves at the difference frequency are discussed next in Section 6.1.4. Following Robertson et al. (2018), we attempt to categorize the sources of uncertainty using the ASME terminology (ASME, 2013) as either random or systematic. Random uncertainties can be assessed with repeated observations; systematic uncertainties create an unknown bias in the results that cannot be quantified through repetitions.



### 6.1.1. Uncertainties of the measured wave amplitudes

Robertson et al. (2018) performed a detailed evaluation of the sources of uncertainty in wave measurements. The sources of random errors identified include the finite precision of the measurement instruments and fluctuations in the environment. In particular, the variation in temperature could affect the conductivity of freshwater and alter the measurements of resistance-type wave probes. Sources of systematic errors, on the other hand, include the positioning of the wave probes, sensor drift, and the variation in the wave properties caused by the tank boundaries. In the present analysis, we directly estimate the uncertainties for the wave amplitudes obtained from an FFT rather than for the instantaneous wave elevation, thus avoiding having to propagate the uncertainties through the FFT analysis following the process described by Betta et al. (2000).

The systematic errors associated with the positioning and orientation of the wave probes are estimated with the help of concurrent measurements from two identical resistance-type wave probes placed side by side near the floater center position at  $y = \pm 0.5$  m basin scale. The differences between  $|A_m|$  (and  $|A_1^* A_2|$ ) determined from the measurements of the two probes are taken as estimations of the systematic errors. The systematic errors obtained in this fashion also provide a measure of the spatial variability of the wave field in the region occupied by the floater, which is also classified as a source of systematic error by Robertson et al. (2018). A nominally 95% confidence interval is obtained by multiplying a coverage factor of 2 to the estimated error. Note that with this approach, the contribution from instrument precision is likely double counted in both the systematic and random uncertainties, resulting in an overconservative estimate.

The second source of uncertainty, sensor drift, has little effect on the results because we are interested in the wave-frequency and difference-frequency components of the waves rather than the mean value.

The positions of the wave maker and the side walls in the physical basin relative to the structure are replicated exactly in the CFD simulations. The water depth is also the same; therefore, the primary concern with the basin boundary effect is with the wave reflection from the downstream beach. The treatment of this source of error is considered separately in Section 6.1.4.

Finally, the random uncertainties of the measured waves are simply estimated from repeated trials. The mean values of  $|A_m|$  and  $|A_1^* A_2|$  from the repeated trials are given by  $\overline{|A_m|}$  and  $\overline{|A_1^* A_2|}$ , respectively (the overbar indicates the averaged values from the repeated trials in the rest of this paper), and the 95% confidence intervals of the means are given by:

$$U_{Rand} = t_{0.95,n-1} \frac{S}{\sqrt{n}} \quad (3)$$

where  $S$  is the standard deviation of the  $n = 3$  repeated trials, and  $t_{0.95,n-1}$  is the two-sided 95% confidence coefficient with  $n - 1$  degrees of freedom from the Student  $t$ -distribution.

The total uncertainties are obtained by combining the systematic uncertainties and the random uncertainties in quadrature. For the difference frequency, we also need the uncertainty of the product of the incident wave amplitudes. This is obtained following the same analysis outlined previously by treating the product of the amplitudes as a single variable. The measured wave amplitudes (and the product of wave amplitudes) near the position where the structure would have been centered are listed in Table 2 along with the estimated random uncertainties,  $U_{Rand}$ , systematic uncertainties,  $U_{Syst}$ , and total uncertainties  $U_{Tot}$ . All values are at full scale. With the present estimates, the systematic uncertainty is higher than the random uncertainty in most cases, which suggests good repeatability of the waves. Further, Wave B2 and Wave B5 with shorter waves tend to have higher systematic uncertainties, which might be related to the increased spatial variability of the wave field in the basin.

**Table 2.** Experimentally measured wave amplitudes and product of wave amplitudes with uncertainties. All values at full scale.

	Low-Freq. Wave [m]				High-Freq. Wave [m]				Product of Wave Amplitudes [m <sup>2</sup> ]			
	$ \overline{A_1} $	$U_{Rand}$	$U_{Syst}$	$U_{Tot}$	$ \overline{A_2} $	$U_{Rand}$	$U_{Syst}$	$U_{Tot}$	$ \overline{A_1^* A_2} $	$U_{Rand}$	$U_{Syst}$	$U_{Tot}$
<b>B1</b>	1.76	±0.010	±0.03	±0.04	1.74	±0.013	±0.03	±0.03	3.05	±0.04	±0.10	±0.11
<b>B2</b>	1.25	±0.009	±0.13	±0.13	1.17	±0.02	±0.15	±0.15	1.46	±0.018	±0.4	±0.4
<b>B3</b>	1.23	±0.012	±0.03	±0.03	1.31	±0.007	±0.002	±0.008	1.61	±0.03	±0.04	±0.04
<b>B4</b>	1.74	±0.03	±0.04	±0.04	1.73	±0.03	±0.03	±0.04	3.01	±0.09	±0.11	±0.14
<b>B5</b>	1.30	±0.008	±0.15	±0.15	1.22	±0.013	±0.07	±0.07	1.58	±0.03	±0.10	±0.10

### 6.1.2. Uncertainties of the measured wave excitations

The random uncertainties of the measured wave loads are similarly estimated from repeated trials using Eq. (3). The random uncertainties thus estimated include the contributions from the random fluctuations in the environment, the incident waves, minor random changes in the behaviors of the instrument, and the instrument precision (Robertson et al., 2018).

Contributors to the systematic error include the geometric errors in the physical model, the orientation and the positioning of the physical model in the basin, and the calibration of the load cells. In the present experimental campaign, strict installation and model geometric tolerances were enforced and checked (Fowler, 2021). For example, when installed in the basin, each column of the model was within ±0.15 degree from vertical. The three columns of the floater were symmetric about the basin center plane with an error in yaw within ±0.07 degree. The draft of each column was within ±2 mm (model scale) from the target value, or 0.5% of the draft. All dimensions of

the physical model—including column height, heave plate height, and diameters—were verified to be within  $\pm 1$  mm (model scale). The corresponding systematic uncertainties of the wave excitation can be estimated by propagating the geometric and model installation variabilities to the wave loads using a Monte Carlo approach with the help of a numerical model, such as a CFD model or a suitable reduced-order model that represents the system well. Alternatively, Robertson et al. (2020a) used a sequential perturbation approach instead of a full Monte Carlo analysis. In the present study, however, the systematic errors from the inaccuracies in the floater model installation and geometry are likely small because of the tight tolerances. The errors are also independent from the other sources of error being considered; therefore, their effects on the final uncertainty estimates should be limited, and further analysis is omitted.

The load cells demonstrated excellent linearity during calibration, with good agreement between the measured loads and the applied loads (Fowler, 2021); therefore, the systematic errors in the calibration coefficients are expected to be small and are also neglected in the present analysis. Note, however, that the load cells were calibrated statically in a dry-bench test. It is possible that the load cells behave slightly differently in the actual dynamic wave environment. In fact, small structural vibrations at frequencies much higher than those of the waves can be observed from the experimental time series (see, e.g., Figure 5). It is unclear, based on the available information, how the dynamic loading might affect the accuracy of the measured wave loads at the lower wave frequencies and the even lower difference frequency; therefore, we neglect this effect in the present uncertainty analysis. Based on this discussion, we consider only the random uncertainties in the measured wave-excitation amplitudes.

As discussed earlier, the reflected waves from the elliptical beach also contribute to errors in the measured wave loads; this contribution is treated separately in Section 6.1.4.

### 6.1.3. Uncertainties of the normalized wave excitations

Neglecting the uncertainties of  $\rho$ ,  $g$ , and  $L$ , the uncertainties in the normalized wave loads,  $U_{\overline{|X|}}$ , are obtained following the standard propagation rule for independent sources of uncertainties (Farrance and Frenkel, 2012):

$$\frac{U_{\overline{|X|}}}{\overline{|X|}} = \sqrt{\left(\frac{U_{\overline{|A|}}}{\overline{|A|}}\right)^2 + \left(\frac{U_{\overline{|F|}}}{\overline{|F|}}\right)^2} \quad (4)$$

In Eq. (4),  $U_{\overline{|A|}}$  and  $U_{\overline{|F|}}$  are the total uncertainties in the magnitudes of the wave amplitudes (or the product of the wave amplitudes) and in the magnitudes of the wave-load amplitudes, respectively.  $F$  and  $A$  represent  $F_j^{(-)}$  and

$A_1^* A_2$  if applied to the difference frequency or  $F_{j,m}$  and  $A_m$  if applied to the wave frequencies, and  $X$  represents either  $X_j^{(-)}$  or  $X_{j,m}$ .

Note that if part of the errors in the measured wave amplitudes and wave excitation are positively correlated, the assumption of independence adopted here will result in conservative uncertainties for the normalized wave loads. A major source of correlated (not necessarily positively) errors between the wave amplitudes and the wave loads is the wave reflection from the elliptical beach in the wave basin, which requires separate consideration (see Section 6.1.4).

The normalized wave-excitation amplitudes in surge and pitch along with the uncertainties estimated using Eq. (4) are listed in Table 3. The waves B1 and B3 have the same frequencies for both wave components; only the wave amplitudes are different. Consistent with our expectation, the normalized wave excitations at the two wave frequencies from B1 and B3 agree with each other up to the estimated uncertainties, lending some confidence to the experimental measurements and the uncertainty estimation. Similar agreement can also be observed with  $\overline{X_{1,1}}$  and  $\overline{X_{5,1}}$  among B1, B3, and B4, which all share the same first (lower) wave frequency (see Table 1).

**Table 3.** Normalized amplitudes of wave excitation on the entire floater with uncertainties. All values at full scale.

	Surge Force			Pitch Moment		
	$\overline{X_1^{(-)}}$	$\overline{X_{1,1}}$	$\overline{X_{1,2}}$	$\overline{X_5^{(-)}}$	$\overline{X_{5,1}}$	$\overline{X_{5,2}}$
<b>B1</b>	0.070±0.004	0.140±0.007	0.116±0.008	0.063±0.003	0.048±0.001	0.059±0.002
<b>B2</b>	0.09±0.02	0.14±0.02	0.08±0.01	0.09±0.02	0.063±0.007	0.042±0.006
<b>B3</b>	0.055±0.002	0.140±0.003	0.116±0.007	0.060±0.002	0.048±0.001	0.059±0.001
<b>B4</b>	0.028±0.002	0.138±0.005	0.144±0.004	0.013±0.001	0.048±0.002	0.057±0.002
<b>B5</b>	0.030±0.002	0.140±0.02	0.128±0.008	0.021±0.002	0.063±0.007	0.062±0.004

#### 6.1.4. Errors from wave reflection and difference-frequency free waves

The wave basin uses an elliptical beach to absorb most of the incident waves; however, the absorption is not perfect, and some wave reflection is unavoidable. Further, spurious, linear, free waves might have been present at the difference frequency because of imperfect wave generation, leading to the contamination of the difference-frequency wave loads. In this section, we first analyze the experimental waves measured at five different positions in the basin using a wave-splitting procedure similar to, e.g., that of Waals (2009). Subsequently, we estimate the corrections needed to remove the effects of the reflected waves and the difference-frequency free waves.

Considering the limited number of wave probes used in the experiment, however, the confidence in the estimated

corrections is limited; therefore, rather than applying the corrections deterministically, they are used to derive additional uncertainties in the normalized wave loads.

The wave-splitting analysis performed is based on two assumptions. First, second-order waves are assumed because we are only interested in the difference-frequency component. Also, according to Méhauté (1976), the normalized wave-height parameters and water-depth parameters of all selected bichromatic waves fall within the applicability of Stokes second-order theory for deep water (the normalized wave-height parameter is conservatively estimated using the sum of the wave heights of the two primary wave components and the longer of the two wave periods,  $(2|A_1| + 2|A_2|)/(gT_1^2)$ , following Lykke Andersen et al. (2019)). Second, long-crested bidirectional waves (forward and backward along the length of the wave basin) are assumed. Waals (2009) recommended the use of two-dimensional wave-splitting analysis for square-shaped ocean-type basins to resolve possible small low-frequency wave components traveling in the transverse direction. This is important if the sway motion/loads of the structure need to be captured. In the present analysis, however, we have a relatively narrow basin, and the sway force and roll moment are not investigated; therefore, it should be adequate to assume bidirectional waves (forward and backward) and neglect any transverse wave components. Also note that, based on Waals (2009), neglecting the transverse components tends to result in an overestimation of the low-frequency free waves in the longitudinal direction, thus overestimating the corresponding error contributions to the wave loads.

#### 6.1.4.1. Wave-splitting analyses of the experimental waves

It is possible to quantify the wave reflection with the help of wave measurements at multiple locations along the length of the basin. At each of the two primary wave frequencies, two long-crested wave trains coexist: one forward propagating from the wave maker to the beach and the other propagating backward; therefore, the wave amplitudes along the length of the basin are given by:

$$A_m(x) = A_m^f e^{-ik_m x} + A_m^b e^{ik_m x}, m = 1, 2 \quad (5)$$

where  $A_m(x)$  is the complex wave amplitude at frequency  $f_m$  as a function of the longitudinal position along the basin,  $x$ . The corresponding wave number,  $k_m$ , estimated from the linear dispersion relation, is accurate up to the second order (Lykke Andersen, 2019).  $A_m^f$  and  $A_m^b$  are, respectively, the constant wave amplitudes of the forward and backward propagating components. From the wave measurements at  $p$  different  $x$ -positions,  $x = x_1, \dots, x_p$ , we

can determine  $A_{m,k} = A_m(x_k)$  using FFT analyses, and a complex linear system of equations can be formed to solve for  $A_m^f$  and  $A_m^b$ :

$$\begin{bmatrix} e^{-ik_mx_1} & e^{ik_mx_1} \\ \vdots & \vdots \\ e^{-ik_mx_p} & e^{ik_mx_p} \end{bmatrix} \begin{bmatrix} A_m^f \\ A_m^b \end{bmatrix} = \begin{bmatrix} A_{m,1} \\ \vdots \\ A_{m,p} \end{bmatrix} \quad (6)$$

In the present experimental campaign, we have  $p = 5$  wave probes (see Figure 3), and the two unknowns  $A_m^f$  and  $A_m^b$  are solved for in the least-squares fashion. Further, to allow for small errors in the wave frequencies, the wave number,  $k_m$ , is allowed to deviate slightly from the value given by the linear wave theory to minimize the least-squares error. For all wave components, the optimal value of  $k_m$  is found within an interval of  $\pm 1.5\%$  from that of the linear theory. Note that the nonlinear amplitude dispersion can also slightly alter the wave number,  $k_m$ , a third-order effect; therefore, the incident and reflected wave components can have slightly different wave numbers because of the different amplitudes (Lykke Andersen et al., 2019). For the bichromatic waves investigated, the changes in wave numbers from this third-order effect are estimated to be less than 1% based on third-order Stokes wave theory for regular waves (neglecting the third-order interaction between the two primary waves) in deep water and are not explicitly considered in the present analysis, which assumes second-order waves.

The corrected incident wave amplitude at the floater position,  $x = 0$ , and frequency,  $f_m$ , with the contribution from the reflected waves removed is given by  $\tilde{A}_m = A_m^f$ . The results from the wave-splitting analysis,  $|A_m^f|$  and  $|A_m^b|$ , are listed in Table 4. The reflection coefficients, defined as  $R_m = |A_m^b|/|A_m^f|$ , are also included for reference. Wave B2 has the highest reflection coefficient, reaching approximately 4%. This is consistent with the wave-basin specification stating that all relevant wave frequencies should have less than or equal to 7% reflection (Fowler, 2021).

**Table 4.** Estimated amplitudes of the forward and backward waves at each wave frequency.

	First (Low-Frequency) Wave Component			Second (High-Frequency) Wave Component		
	$ A_1^f $	$ A_1^b $	$R_1 =  A_1^b / A_1^f $	$ A_2^f $	$ A_2^b $	$R_2 =  A_2^b / A_2^f $
<b>B1</b>	1.695	0.013	0.8%	1.730	0.016	1.0%
<b>B2</b>	1.202	0.052	4.3%	1.211	0.047	3.9%
<b>B3</b>	1.187	0.009	0.7%	1.290	0.027	2.1%
<b>B4</b>	1.687	0.002	0.1%	1.726	0.050	2.9%
<b>B5</b>	1.240	0.019	1.5%	1.243	0.009	0.7%

At the difference frequency, the wave splitting is more complicated because of the presence of forward and backward linear free waves in addition to the second-order bound waves from the interaction between any two primary wave components and their reflections with different frequencies. The free waves at the difference

frequency likely came from imperfect wave generation and are a source of contamination (Waals, 2009). This issue was first identified and analyzed in the CFD analyses of OC6 Phase Ib by Wang et al. (2021a, 2021b). To quantify the difference-frequency wave components, a modified wave-splitting procedure is adopted. Based on the wave elevation of general directional second-order seas (Sharma and Dean, 1982), there are potentially up to six wave components at the difference frequency assuming bidirectional waves (forward and backward along the length of the basin):

$$A_d(x) = A_d^f e^{-ik_d x} + A_d^b e^{ik_d x} + A_b^f e^{-ik_b x} + A_b^b e^{ik_b x} + A_p^f e^{-ik_p x} + A_p^b e^{ik_p x} \quad (7)$$

where  $A_d(x)$  is the wave amplitude at the difference frequency,  $f_d = f_2 - f_1$ . The first two terms on the right-hand side of Eq. (7) are the forward and backward linear free waves at the difference frequency with wave number,  $k_d$ , given by the linear dispersion relation. The third and fourth terms are the forward and backward bound waves with the wave number  $k_b = k_2 - k_1$ , where  $k_1$  and  $k_2$  are the wave numbers corresponding to frequencies  $f_1$  and  $f_2$  computed from the linear-wave dispersion relation. These waves are generated from the interactions between the two incident primary waves and between the two reflected primary waves, respectively. The last two terms are bound waves with wave number  $k_p = k_1 + k_2$ , which are generated from the interaction between one incident primary wave and one reflected primary wave at the other frequency. The six wave components are characterized by the complex amplitudes  $A_d^f$ ,  $A_d^b$ ,  $A_b^f$ ,  $A_b^b$ ,  $A_p^f$ , and  $A_p^b$ .

Because only five wave probes were used in the experiment, there is not enough information to solve for all six unknown wave amplitudes in Eq. (7); therefore, the nonlinear bound waves associated with one or both reflected primary waves are assumed to be small and are neglected in the analysis. This simplification, which was also adopted by Waals (2009), is justified by the smallness of the reflected primary waves (as shown in Table 4) and the quadratic nature of the neglected nonlinear wave components. The neglected wave components are expected to be at least an order of magnitude smaller than the three retained second-order components— $A_d^f$ ,  $A_d^b$ , and  $A_b^f$ —in Eq. (7) and are thus safely neglected. With this simplification, a linear system of equations similar to Eq. (6) can be formed to solve for the three unknowns— $A_d^f$ ,  $A_d^b$ , and  $A_b^f$ —using  $A_d(x)$  measured at five different locations along the length of the basin. This is essentially the same wave-splitting analysis previously successfully applied to the CFD investigation of the OC6 Phase Ib project (Wang et al., 2021a, 2021b).

As an example, the difference-frequency wave-splitting analysis for Wave B4 resulted in  $|A_d^f| = 0.026$  m,  $|A_d^b| = 0.025$  m, and  $|A_b^f| = 0.013$  m. As a check, in Figure 7, the complex difference-frequency wave amplitudes directly obtained from the wave-probe measurements are compared to the reconstructed amplitudes obtained using Eq. (7) (neglecting the last three terms on the right-hand side) with  $A_d^f$ ,  $A_d^b$ , and  $A_b^f$  from the wave-splitting analysis. Overall, the reconstructed wave amplitude fits the readings from the five wave probes reasonably well with some deviations between the two likely caused by errors in the wave measurements, the neglected terms in Eq. (7), and/or some other imperfections in the experimental waves. The confidence in this wave-splitting analysis could have been higher if more wave probes had been used in the experimental campaign.

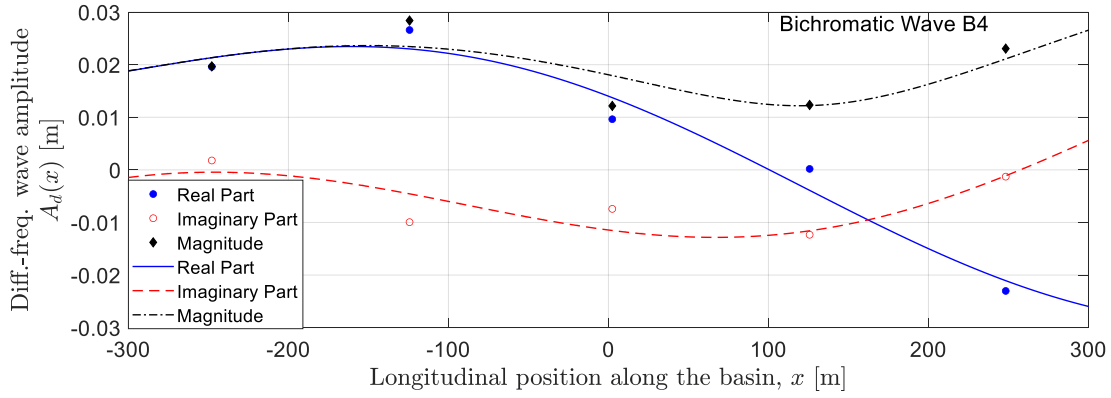


**Figure 7.** Comparison of the difference-frequency wave amplitude of Wave B4 obtained directly from the wave-probe measurements (symbols) and that reconstructed from  $A_d^f$ ,  $A_d^b$ , and  $A_b^f$  using Eq. (7) (lines). The wave probes are the ones shown in Figure 3. All values are at full scale.

#### 6.1.4.2. Corrections to the normalized wave excitation

To estimate the errors in the normalized wave excitations, we first attempt to derive corrected wave loads by removing the contributions from the reflected waves and the difference-frequency free waves. At the two primary wave frequencies, this is straightforward with the help of linear potential-flow theory:

$$\tilde{F}_{j,m} = F_{j,m} - A_m^b X_{p,j}(f_m, \beta_b) \quad (8)$$

where  $\tilde{F}_{j,m}$  is the corrected amplitude of the wave excitation at wave frequency  $f_m$  in mode  $j$ . The contribution from the reflected wave is estimated with  $X_{p,j}$ , the unit-amplitude wave excitation in mode  $j$  from the linear potential-flow theory, which depends on the frequency and wave direction  $\beta_b = 180^\circ$  for the reflected wave.

The correction to the wave excitation at the difference frequency,  $F_j^{(-)}$ , is given by:



$$\begin{aligned}\tilde{F}_j^{(-)} = F_j^{(-)} - 2A_1^{f*} A_2^b X_{p,j}^{(-)}(f_2, f_1; \beta_b, \beta_f) - 2A_1^{b*} A_2^f X_{p,j}^{(-)}(f_2, f_1; \beta_f, \beta_b) \\ - A_d^f X_{p,j}(f_d, \beta_f) - A_d^b X_{p,j}(f_d, \beta_b)\end{aligned}\quad (9)$$

where  $\beta_f = 0^\circ$  is the angle of the incident waves, and  $X_{p,j}^{(-)}$  is the difference-frequency quadratic wave excitation estimated from the second-order potential-flow theory. Although, admittedly, second-order potential-flow QTFs do not always provide reliable estimates of quadratic wave excitations (this is part of the motivation of the present investigation), we nevertheless relied on them for uncertainty analysis in the absence of better estimates. Further, the QTFs tend to perform better when the wave amplitudes are small because of reduced viscous effects. In Eq. (9), the quadratic terms always involve one reflected wave component, which tends to be very small, and we hope that this will lead to more reasonable estimates of the quadratic excitation by the QTFs that are, in conjunction with a coverage factor, adequate for uncertainty estimation. The second and third terms on the right-hand side of Eq. (9) account for the contributions from the interaction between the incident wave at one primary frequency and the reflected wave at the other. The last two terms account for the contributions from the contaminating difference-frequency free waves. The contribution from the interaction between the two reflected waves at the primary wave frequencies is small and is neglected. In the present work, the values of the linear and quadratic wave excitation,  $X_{p,j}$  and  $X_{p,j}^{(-)}$ , are all computed using the commercial boundary-element-method software WAMIT Version 6.107S (Lee, 1995).

The normalized amplitudes of the wave excitation after the correction for wave reflection and difference-frequency wave contamination,  $\tilde{X}_j^{(-)}$  and  $\tilde{X}_{j,m}$ , are computed from Eq. (1) and Eq. (2) by replacing  $A_m$  with  $\tilde{A}_m$  and replacing  $F_{j,m}$  and  $F_j^{(-)}$  with  $\tilde{F}_{j,m}$  and  $\tilde{F}_j^{(-)}$ . Because of the limited confidence in the estimated correction (partially a consequence of the limited number of wave probes available for the wave-splitting analysis), however, we do not use the corrected values directly for validating the CFD simulations; rather, we use the difference between the normalized wave excitations before and after the correction to estimate an uncertainty,  $U_w$ , to account for the effects of wave reflection and wave contamination. Consistent with our estimations of other systematic uncertainties, a coverage factor of 2 is used with the intention of obtaining a nominally 95% confidence level. More specifically, we have  $U_w = 2 \left| \left| \tilde{X}_j^{(-)} \right| - \left| X_j^{(-)} \right| \right|$  for the difference-frequency wave loads and  $U_w = 2 \left| \left| \tilde{X}_{j,m} \right| - \left| X_{j,m} \right| \right|$  for the wave-frequency loads. The uncertainty,  $U_w$ , provides a measure of the systematic errors in the normalized wave loads caused by the presence of wave reflection from the downstream beach and the presence of contaminating difference-

frequency free waves in the basin.  $U_w$  is combined with the uncertainty from Eq. (4) in quadrature to obtain the total uncertainties in  $|X_j^{(-)}|$  and  $|X_{j,m}|$ . The normalized wave-excitation amplitudes before and after the correction are shown in Table 5 and Table 6 along with  $U_w$ .

**Table 5.** The normalized amplitudes of total surge force before and after correction and  $U_w$ . All values at full scale.

	Difference Frequency			1 <sup>st</sup> (Low) Wave Frequency			2 <sup>nd</sup> (High) Wave Frequency		
	$ X_1^{(-)} $	$ \tilde{X}_1^{(-)} $	$U_w$	$ X_{1,1} $	$ \tilde{X}_{1,1} $	$U_w$	$ X_{1,2} $	$ \tilde{X}_{1,2} $	$U_w$
<b>B1</b>	0.070	0.070	$\pm 0.0006$	0.140	0.146	$\pm 0.013$	0.116	0.117	$\pm 0.004$
<b>B2</b>	0.09	0.08	$\pm 0.004$	0.14	0.147	$\pm 0.018$	0.08	0.081	$\pm 0.008$
<b>B3</b>	0.055	0.057	$\pm 0.004$	0.140	0.146	$\pm 0.012$	0.116	0.120	$\pm 0.008$
<b>B4</b>	0.028	0.030	$\pm 0.006$	0.138	0.142	$\pm 0.009$	0.144	0.148	$\pm 0.01$
<b>B5</b>	0.030	0.032	$\pm 0.004$	0.140	0.148	$\pm 0.018$	0.128	0.125	$\pm 0.006$

**Table 6.** The normalized amplitudes of total pitch moment before and after correction and  $U_w$ . All values at full scale.

	Difference Frequency			1 <sup>st</sup> (Low) Wave Frequency			2 <sup>nd</sup> (High) Wave Frequency		
	$ X_5^{(-)} $	$ \tilde{X}_5^{(-)} $	$U_w$	$ X_{5,1} $	$ \tilde{X}_{5,1} $	$U_w$	$ X_{5,2} $	$ \tilde{X}_{5,2} $	$U_w$
<b>B1</b>	0.063	0.066	$\pm 0.006$	0.048	0.051	$\pm 0.005$	0.059	0.060	$\pm 0.002$
<b>B2</b>	0.09	0.09	$\pm 0.003$	0.063	0.068	$\pm 0.01$	0.042	0.040	$\pm 0.005$
<b>B3</b>	0.060	0.063	$\pm 0.007$	0.048	0.050	$\pm 0.004$	0.059	0.060	$\pm 0.003$
<b>B4</b>	0.013	0.013	$\pm 0.002$	0.048	0.050	$\pm 0.003$	0.057	0.059	$\pm 0.004$
<b>B5</b>	0.021	0.021	$\pm 0.001$	0.063	0.067	$\pm 0.008$	0.062	0.061	$\pm 0.002$

**Table 7.** Normalized amplitudes of total wave excitation on the entire floater with total uncertainties. All values at full scale.

	Surge Force			Pitch Moment		
	$ X_1^{(-)} $	$ X_{1,1} $	$ X_{1,2} $	$ X_5^{(-)} $	$ X_{5,1} $	$ X_{5,2} $
<b>B1</b>	$0.070 \pm 0.004$	$0.140 \pm 0.014$	$0.116 \pm 0.009$	$0.063 \pm 0.007$	$0.048 \pm 0.005$	$0.059 \pm 0.003$
<b>B2</b>	$0.09 \pm 0.02$	$0.14 \pm 0.03$	$0.08 \pm 0.02$	$0.09 \pm 0.03$	$0.063 \pm 0.012$	$0.042 \pm 0.008$
<b>B3</b>	$0.055 \pm 0.004$	$0.140 \pm 0.012$	$0.116 \pm 0.011$	$0.060 \pm 0.007$	$0.048 \pm 0.005$	$0.059 \pm 0.003$
<b>B4</b>	$0.028 \pm 0.006$	$0.138 \pm 0.010$	$0.144 \pm 0.011$	$0.013 \pm 0.002$	$0.048 \pm 0.004$	$0.057 \pm 0.004$
<b>B5</b>	$0.030 \pm 0.004$	$0.140 \pm 0.03$	$0.128 \pm 0.009$	$0.021 \pm 0.002$	$0.063 \pm 0.011$	$0.062 \pm 0.004$

The values of  $U_w$  are often comparable to or larger than the uncertainties in Table 3, with a few exceptions, which means that the errors from the wave reflection and the wave contamination are not negligible and should be included in a comprehensive uncertainty analysis whenever possible. The total uncertainties of the various quantities needed to validate the CFD simulations are listed in Table 7.

## 6.2. Uncertainties for CFD simulations

In the present paper, the uncertainties in the CFD solutions are all assessed following the procedures of Wang et al. (2021a). The discretization uncertainties are estimated based on the recommended practices from the literature (see, e.g., Eça and Hoekstra (2014), Eça (2006), and Wang et al. (2018)). The iterative error can be estimated from an extrapolation-type approach (Eça et al., 2018, 2019). The round-off error can often be neglected with the use of double-precision computation (Eça and Hoekstra, 2009), as is the case with the present investigation. Because of the

high computing cost for a systematic convergence study, numerical uncertainties are estimated for only the NREL solutions and for only two of the five bichromatic waves, B1 and B4, chosen for validation against the experiment.

## 7. Validation of the Numerical Simulations

The CFD predictions from the OC6 participants are validated against the experimental results. Both total wave excitation on the entire floater, Section 7.1, and the separate wave loads on each column, Section 7.2, are considered. Although not strictly the case, the vast majority of the CFD simulations were completed before the experimental campaign; therefore, the comparison presented here can be considered as mostly a blind validation.

In the CFD simulations, many virtual wave probes were placed along the centerline of the numerical domain; therefore, the wave-splitting analysis could be performed with much higher confidence. As a result, the difference-frequency wave excitations from the CFD simulations shown here have all been corrected using Eq. (9) deterministically (instead of as uncertainties, as was done with the experimental results), with the second and third terms on the right-hand side neglected because of negligible reflection of the two primary waves (Wang et al., 2021a, 2021b). This correction has been found to significantly improve the consistency of the CFD results (Wang et al., 2021b). For participants directly using second-order bichromatic-wave theory for wave generation in the CFD simulations (see appendix), this correction has negligible effects on the results and is not necessary.

In Figure 8 through Figure 15, EXP stands for the experimental results. All other labels correspond to the CFD results from the various OC6 CFD participants. The only exception, TUHH, is based on a time-domain, 3D, lower-order panel method, *panMARE* (Ferreira González et al., 2021), which solves the potential flow field and free-surface elevation at each time step. Second-order wave potential and contributions from Morison drag are included. Finally, the predictions from the second-order potential-flow theory are also included for reference, shown as hatched bars.

### 7.1. Total wave excitations on the entire floater

Three of the bichromatic wave cases are reviewed in this section: B1, B3, and B4. The CFD uncertainties are evaluated only for B1 and B4. These two cases are considered more important because the two wave frequencies are close to the irregular-wave peak frequency used in the previous OC6 Phase Ia study with engineering models (Robertson et al., 2020b), which demonstrated the underprediction of low-frequency excitation and response. The

1  
2  
3  
4 difference frequencies of B1 and B4 are close to the pitch and surge resonance frequencies of the FOWT,  
5  
6 respectively. In addition to B1 and B4, an informal comparison of the CFD and experimental results for B3 is also  
7  
8 included without uncertainties for the NREL CFD solutions. B3 is focused on because it is the case with the most  
9  
10 consistent CFD predictions across all participants.  
11

12 The amplitudes of the global surge force and pitch moment on the entire floater are shown in Figure 8, Figure 9,  
13  
14 and Figure 10 for waves B1, B3, and B4, respectively. In Figure 8a, the CFD simulations and the experiment  
15  
16 generally provide consistent values for the wave-frequency surge force, with the majority of the CFD solutions  
17  
18 falling within the experimental uncertainties. The differences between the CFD/experimental results and the  
19  
20 predictions of the linear potential-flow theory, represented by the hatched bars, are also small, indicating negligible  
21  
22 viscous excitation in surge at the wave frequencies. At the difference frequency, the NREL CFD solution for the  
23  
24 nonlinear surge force has a relatively wide uncertainty interval, which reflects the difficulties in obtaining an  
25  
26 accurate numerical prediction for the small nonlinear wave loads. The higher uncertainty of the NREL CFD result is  
27  
28 also consistent with the level of scatter demonstrated by the other CFD solutions. Nevertheless, the NREL CFD  
29  
30 solution is considered validated by the experimental measurements up to the estimated uncertainties. More  
31  
32 importantly, both the experiment and the CFD simulations show that the second-order potential-flow theory, the  
33  
34 hatched bars, severely underpredicts the difference-frequency surge force, with major consequences on the  
35  
36 prediction of low-frequency surge motion. The potential-flow panel method of TUHH also obtained a good  
37  
38 prediction of the difference-frequency surge force with the help of Morison drag components.  
39  
40

41 In Figure 8b, the majority of the CFD predictions of the difference-frequency pitch moment fall within the  
42  
43 estimated experimental uncertainty range. As with the surge force, second-order potential-flow theory also  
44  
45 underpredicts the nonlinear pitch moment on the floater when compared to the experiment and the CFD simulations.  
46  
47 Although the underprediction is not as severe as with the surge force, the difference in pitch moment is still  
48  
49 significant, with the potential-flow prediction falling outside the uncertainty bands of the experiment and the NREL  
50  
51 CFD simulation. On the other hand, the linear potential-flow theory, CFD simulations, and the experiment all  
52  
53 provide similar values for the wave-frequency pitch moments.  
54  
55  
56  
57  
58  
59  
60  
61  
62  
63  
64  
65

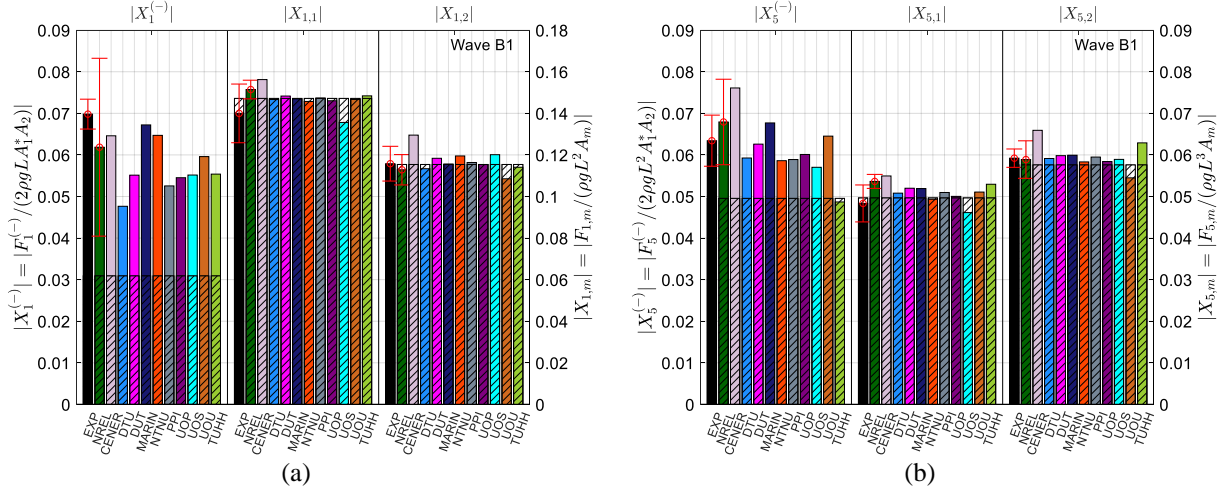


**Figure 8.** Normalized wave-exciting (a) surge force and (b) pitch moment on the entire floater at the difference and the two wave frequencies for Wave B1. EXP is the experimental result. The hatched bars are predictions of potential-flow theory, with second-order solution for the difference frequency.

The CFD results for Wave B3, which has the same wave frequencies as B1 but lower wave heights, are shown in Figure 9. These results are considerably more consistent than those for B1 and are also better aligned with the measurements, especially at the difference frequency. The improved agreement among the CFD results for B3 likely comes from the lower wave amplitudes, which weaken the viscous effects, such as the flow separation from the sharp corners of the heave plates and the drag force on the upper columns. These flow structures are generally more challenging to capture accurately in CFD simulations because of the numerical resolution required. The CFD predictions are generally in good agreement with the experimental measurements. As shown in Figure 9a, approximately half of the CFD predictions for the difference-frequency surge force fall within the estimated uncertainty range of the experimental result and are thus validated. This is especially encouraging because the experimental uncertainty range of the nonlinear surge force is relatively narrow for B3. The TUHH solution slightly overpredicts the difference-frequency surge force, suggesting some model tuning is needed for different wave amplitudes. Nevertheless, the prediction is still acceptable, and it should be possible to have a single model that works reasonably well for a range of wave amplitudes. In Figure 9b, all CFD predictions of the difference-frequency pitch moment fall within the uncertainty range of the experimental measurement. As with B1, the second-order potential-flow theory underpredicts the difference-frequency surge force and pitch moment, with the underprediction of the surge force being more severe. One interesting observation is that the CFD simulations by IFPEN and UOP, which use a free-slip condition on the surface of the structure, also compare well with the experimental

measurements and other CFD solutions, suggesting that resolving the shear layer numerically might not be critical for some wave conditions. This observation is consistent with the conclusions from prior investigations (Wang et al., 2021b; Clément et al., 2020).

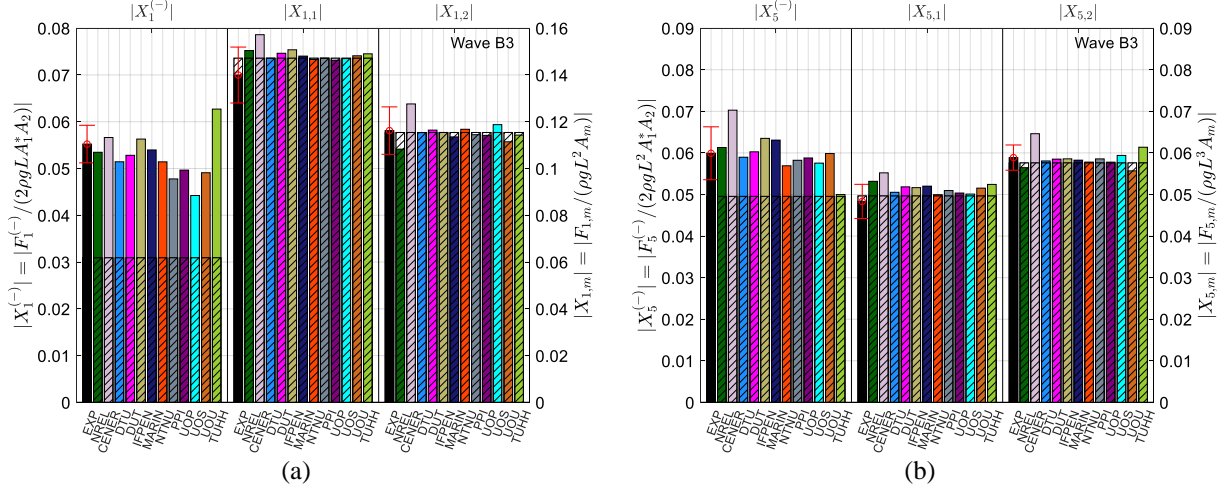


**Figure 9.** Normalized wave-exciting (a) surge force and (b) pitch moment on the entire floater at the difference and the two wave frequencies for Wave B3. EXP is the experimental result. The hatched bars are predictions of potential-flow theory, with second-order solution for the difference frequency.

For Wave B4, the CFD predictions of the difference-frequency surge force show more scatter (Figure 10a). This is unfortunate because the difference frequency of B4 is close to the surge resonance frequency, at which a consistent prediction of the nonlinear surge force is most valuable. Still, approximately half of the CFD predictions fall within the experimental uncertainty band, and there is limited overlap between the experimental uncertainty range and the uncertainty interval of the NREL CFD solution. Both observations suggest a limited degree of agreement between the experiment and the CFD results. Further, both the experimental measurements and the CFD predictions of the difference-frequency surge force are higher than the second-order potential-flow prediction by at least an order of magnitude. The increased surge force is also captured by the TUHH solution with added Morison drag, which appears to suggest that the difference-frequency surge force primarily comes from viscous drag in this case. This conjecture is consistent with the fact that both IFPEN and UOP simulations with a free-slip condition on the structure slightly underpredict the nonlinear surge force by possibly underestimating the viscous effects. Note that this observation contrasts with that from waves B1 and B3 (Figure 8 and Figure 9) when the contribution from viscous drag to the nonlinear surge force is not as dominant, and both IFPEN and UOP solutions produce good predictions.

In Figure 10b, the CFD predictions of the difference-frequency pitch moment also show more scatter when compared to the two previous wave conditions. It appears that it is generally difficult to obtain accurate and consistent predictions at the very low surge resonance frequency of 0.01 Hz, compared to the higher pitch resonance frequency of 0.032 Hz. This is partially because the absolute magnitudes of the difference-frequency wave excitations tend to be even lower at the surge resonance frequency. Still, as with the two previous wave conditions, the potential-flow prediction of the difference-frequency pitch moment is below the lower uncertainty bounds of the experiment and the NREL CFD solution, suggesting the potential-flow theory is consistently underpredicting the nonlinear pitch moment.

**Figure 10.** Normalized wave-exciting (a) surge force and (b) pitch moment on the entire floater at the difference and the two wave frequencies for Wave B4. EXP is the experimental result. The hatched bars are predictions of potential-flow theory, with second-order solution for the difference frequency.

A more detailed validation can be performed by comparing the wave excitation on the upstream and starboard columns separately. The difference-frequency surge forces on the upstream and starboard columns with Wave B1 are shown in Figure 11. The magnitudes of the surge force, Figure 11a, are mostly consistent between the experiment and the CFD predictions, lending confidence to the CFD results. Second-order potential-flow theory severely underpredicts the surge forces on the upstream column and, to a lesser degree, on the starboard column; however, in Figure 11b, the phases of the surge forces from the potential-flow theory are mostly consistent with the experimental and CFD results.

Figure 12 shows the difference-frequency surge force on each column for Wave B3, which has the same wave frequencies as B1 but lower amplitudes. In terms of the magnitudes of the surge excitation, the CFD predictions are highly consistent, with most of the predictions falling within the uncertainty range of the experimental result: therefore, we consider this a successful validation. The TUHH solution significantly overpredicted the difference-frequency surge force on the upstream column, leading to the overprediction of the global force in Figure 9a.

With Wave B4, the CFD predictions of the difference-frequency surge force on each column, shown in Figure 13, show significant scatter, especially with  $|X_1^{(-)}|$  on the upstream column. Consistent with the scatter, a high uncertainty is also estimated for the NREL CFD solution for  $|X_1^{(-)}|$  on the upstream column. In this case, the high total uncertainty is dominated by the contribution from spatial discretization (Wang et al., 2021a), which means that the mesh resolution is the limiting factor of numerical accuracy. Interestingly, the experiment also shows large uncertainty here, with  $U_w$  (see Section 6.1.4) being the dominant contributor; therefore, issues with the quality of the incident waves, including the presence of wave reflection from downstream and the contaminating linear waves at the difference frequency, are the limiting factors to experimental accuracy. Finally, it can be observed again that both IFPEN and UOP simulations with a free-slip condition on the structure underpredict the difference-frequency surge force, especially on the upstream column, which points to the importance of accurately capturing viscous effects for this load case.

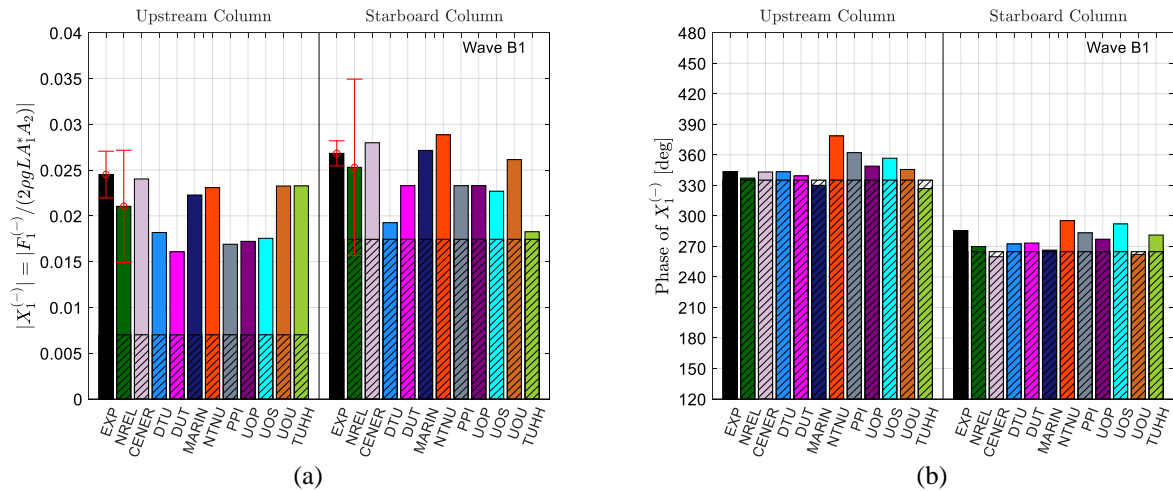


**Figure 11.** The (a) magnitude and (b) phase of the normalized wave-exciting surge force on each column at the difference frequency for Wave B1. EXP is the experimental result. The hatched bars are predictions of the second-order potential-flow theory.



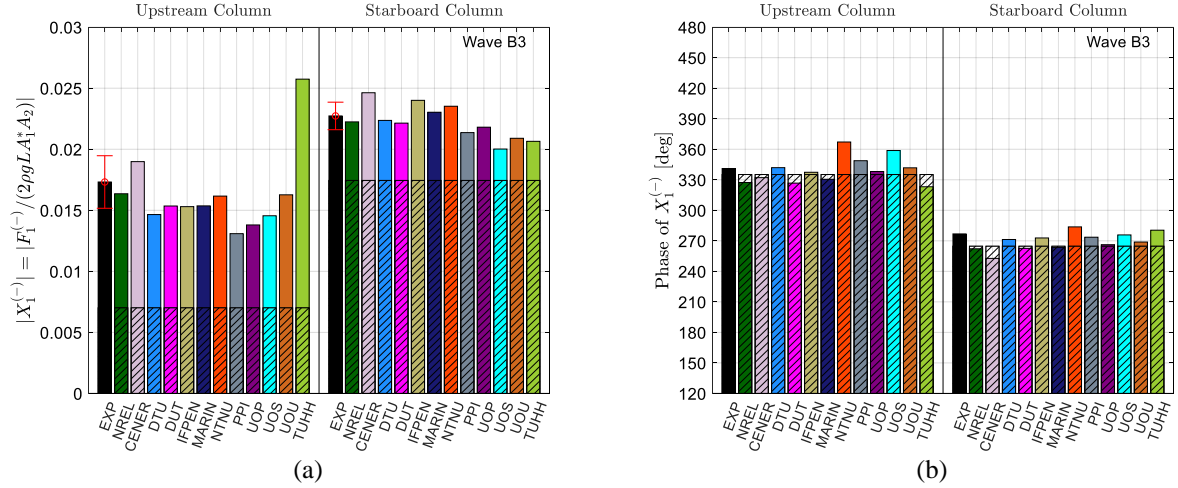


**Figure 12.** The (a) magnitude and (b) phase of the normalized wave-exciting surge force on each column at the difference frequency for Wave B3. EXP is the experimental result. The hatched bars are predictions of the second-order potential-flow theory.

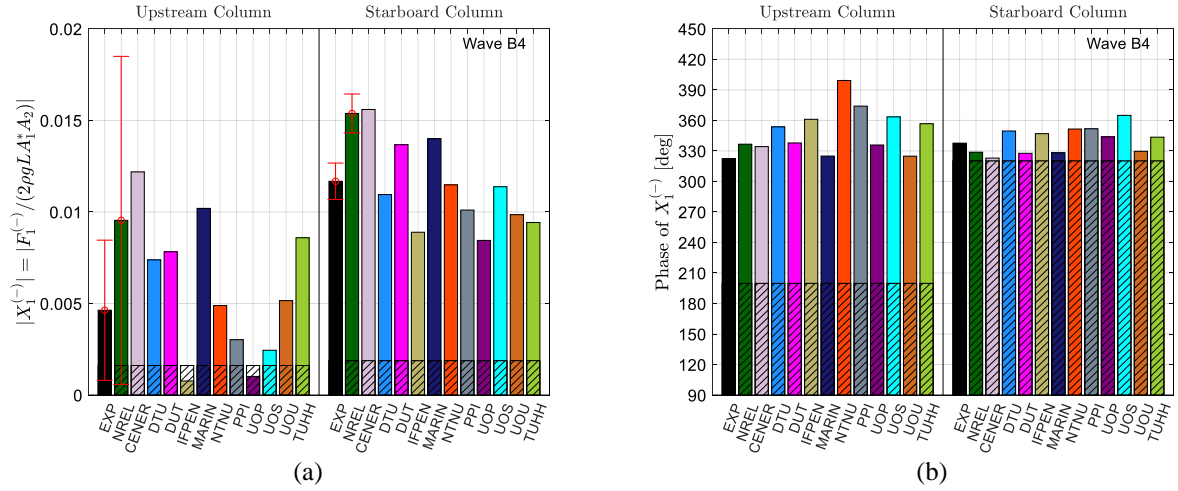


**Figure 13.** The (a) magnitude and (b) phase of the normalized wave-exciting surge force on each column at the difference frequency for Wave B4. EXP is the experimental result. The hatched bars are predictions of the second-order potential-flow theory.

The uncertainties of the surge force on the starboard column are much smaller for both the NREL simulation and the experiment. Unfortunately, the uncertainty bands do not overlap, which suggests that the NREL CFD prediction is not validated; however, the experimental value of  $|X_1^{(-)}|$  on the starboard column approximately falls in the middle of the scatter of the various CFD solutions, and the predictions from several participants fall within the

uncertainty range of the experimental result, indicating some agreement between the experiment and the CFD simulations.

Despite the scatter in the CFD predictions, the second-order potential-flow theory clearly underpredicts the difference-frequency surge force on both columns when compared to the experiment and the CFD predictions. Further, the potential-flow results show  $X_1^{(-)}$  on the upstream and starboard columns as being approximately one-third of a period out of phase, which would result in partial cancellation between the surge force on the upstream column and the two rear columns. In contrast, the experiment indicates that  $X_1^{(-)}$  on the upstream and rear columns are almost in phase, a behavior consistently captured by all CFD solutions.

The large differences in  $|X_1^{(-)}|$  between the potential-flow theory and the experiment/CFD predictions are most likely caused by the viscous drag on the structure. This is hinted by the fact that the potential-flow simulation from TUHH mostly captures the difference-frequency surge force and, more importantly, the phase of the surge force on the upstream column with the help of added Morison drag. It appears that at the surge resonance frequency, the nonlinear surge excitation primarily comes from viscous drag, not second-order wave diffraction. The relatively high contribution from the viscous drag, which is harder to capture accurately with numerical simulations compared to wave diffraction, might also partially explain the increased uncertainties in the CFD solutions.

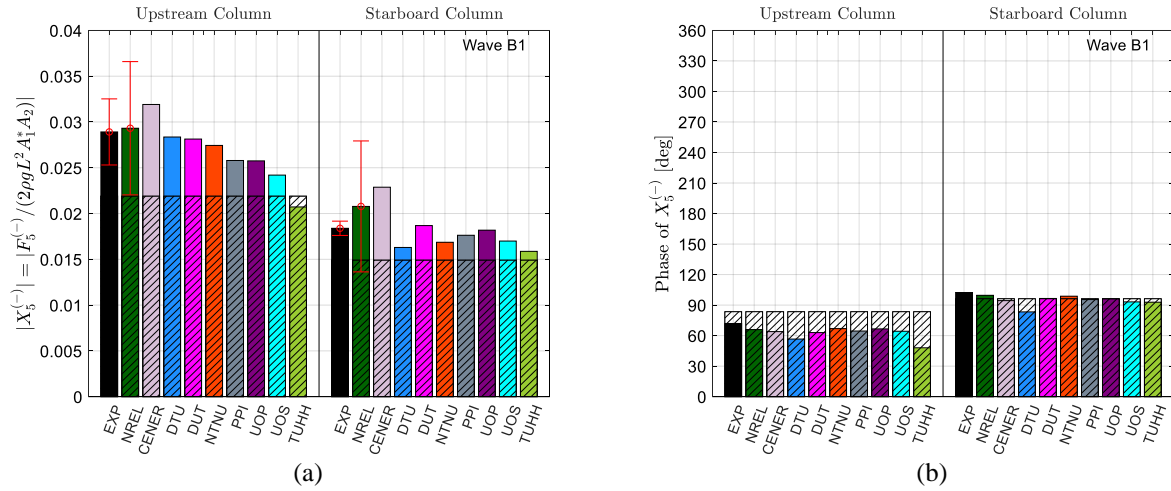


**Figure 14.** The (a) magnitude and (b) phase of the normalized wave-exciting pitch moment on each column at the difference frequency for Wave B1. EXP is the experimental result. The hatched bars are predictions of the second-order potential-flow theory.

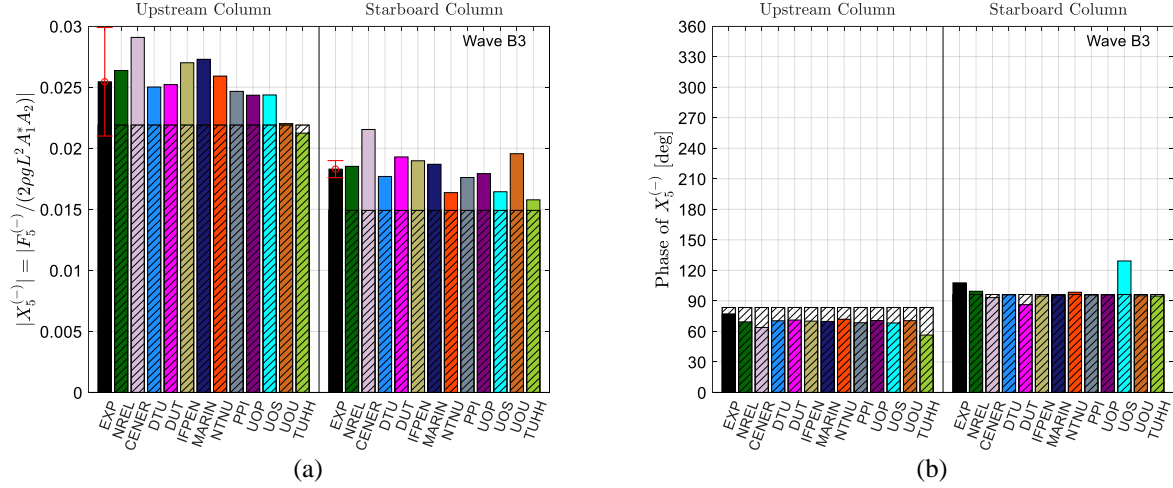


**Figure 15.** The (a) magnitude and (b) phase of the normalized wave-exciting pitch moment on each column at the difference frequency for Wave B3. EXP is the experimental result. The hatched bars are predictions of the second-order potential-flow theory.

The difference-frequency pitch moments on the upstream and starboard columns are shown in Figure 14 and Figure 15 for waves B1 and B3, of which the difference frequency is close to the pitch resonance frequency. Overall, the experiment agrees with the CFD results for both wave conditions. The underprediction of the pitch moment by the potential-flow theory is not as significant (Figure 14a and Figure 15a); the differences between the potential-flow predictions and the experiment/CFD results are sometimes comparable to the uncertainties in the latter. The phases of the pitch moments (Figure 14b and Figure 15b) from the experiment and the CFD solutions also mostly agree; a small phase shift relative to the potential-flow theory is consistently observed for the pitch moment on the upstream column.

## 8. Comparison to Second-Order Potential-Flow QTFs

The difference-frequency QTFs for the surge force and pitch moment on the entire floater from second-order potential-flow theory are shown in Figure 16. The two off-diagonal lines mark the wave frequency pairs that yield a difference frequency close to the surge and pitch resonance frequencies of the FOWT. The different symbols along the two lines mark the frequency pairs associated with the five bichromatic waves investigated. The magnitudes of the QTFs along these two diagonal cuts are shown in Figure 17 along with the results from the experiment and the CFD simulations.

With Wave B4, the difference-frequency surge force from the potential-flow QTF is an order of magnitude below the CFD predictions and the experimental measurements near the surge resonance frequency of 0.01 Hz (see Figure 17a). When the frequency of the first wave component,  $f_1$ , drops below approximately 0.1 Hz, the QTF predicts almost no surge force. It is likely that over this entire frequency range, viscous drag becomes the dominant source of nonlinear low-frequency surge force, whereas the second-order wave diffraction has negligible contribution.

Near the pitch resonance frequency of 0.032 Hz (see Figure 17b), the potential-flow QTF underpredicts the surge force by approximately a factor of 2 compared to the CFD and experimental results for B1 and B3, suggesting second-order wave diffraction and viscous excitation are of comparable importance. By comparing B5 to B4 and B2 to B1/B3, it appears that the relative difference between the potential-flow QTF and the experiment/CFD simulations diminishes with higher wave frequencies and/or lower wave amplitudes.

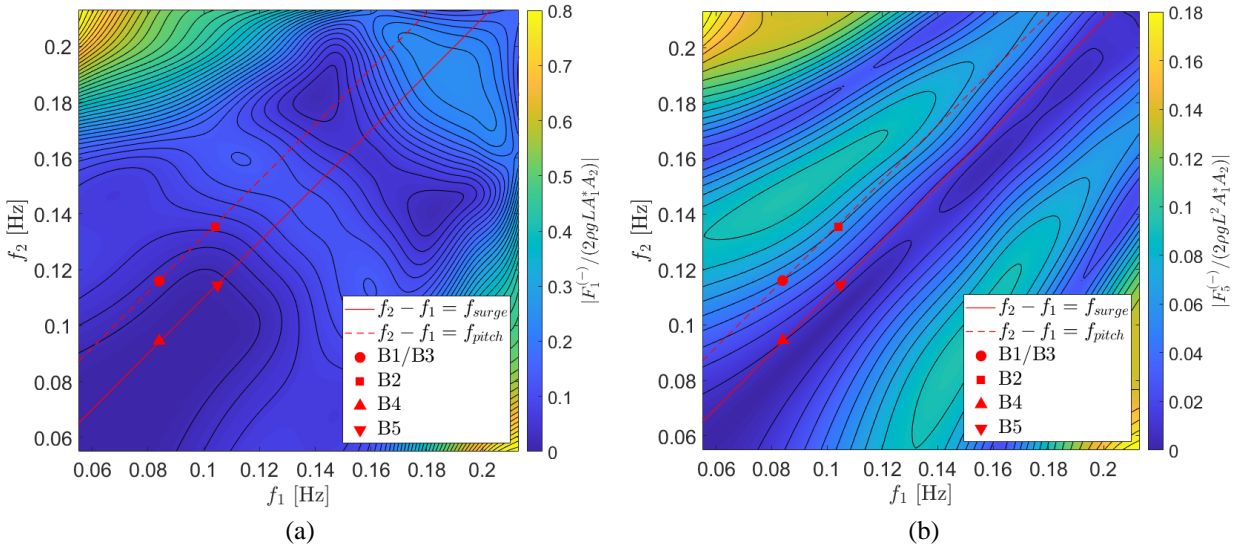


**Figure 16.** Magnitudes of the quadratic transfer functions (QTFs) for the difference-frequency (a) surge force and (b) pitch moment on the entire floater from second-order potential-flow theory. Increments in the contour levels are (a) 0.02 and (b) 0.04. The solid and dashed off-diagonal lines mark the frequency pairs, where the difference frequency is at the surge resonance frequency,  $f_{surge}$ , and the pitch resonance frequency,  $f_{pitch}$ , respectively. The frequency pairs of the five bichromatic waves investigated are marked with different symbols.

Relative to the experiment, the potential-flow QTF underpredicts the difference-frequency pitch moment by 20% to 40% (see Figure 17c and Figure 17d). The difference between the QTF and the experimental/CFD results are most likely caused by the viscous drag on the heave plates not considered in the potential-flow model.

Finally, the amplitude dependence of the normalized difference-frequency surge force can be observed by comparing the experimental measurements for B1 and B3, for which the experimental uncertainty bands do not overlap (see Figure 17b). This amplitude dependence is also captured by the CFD simulations.

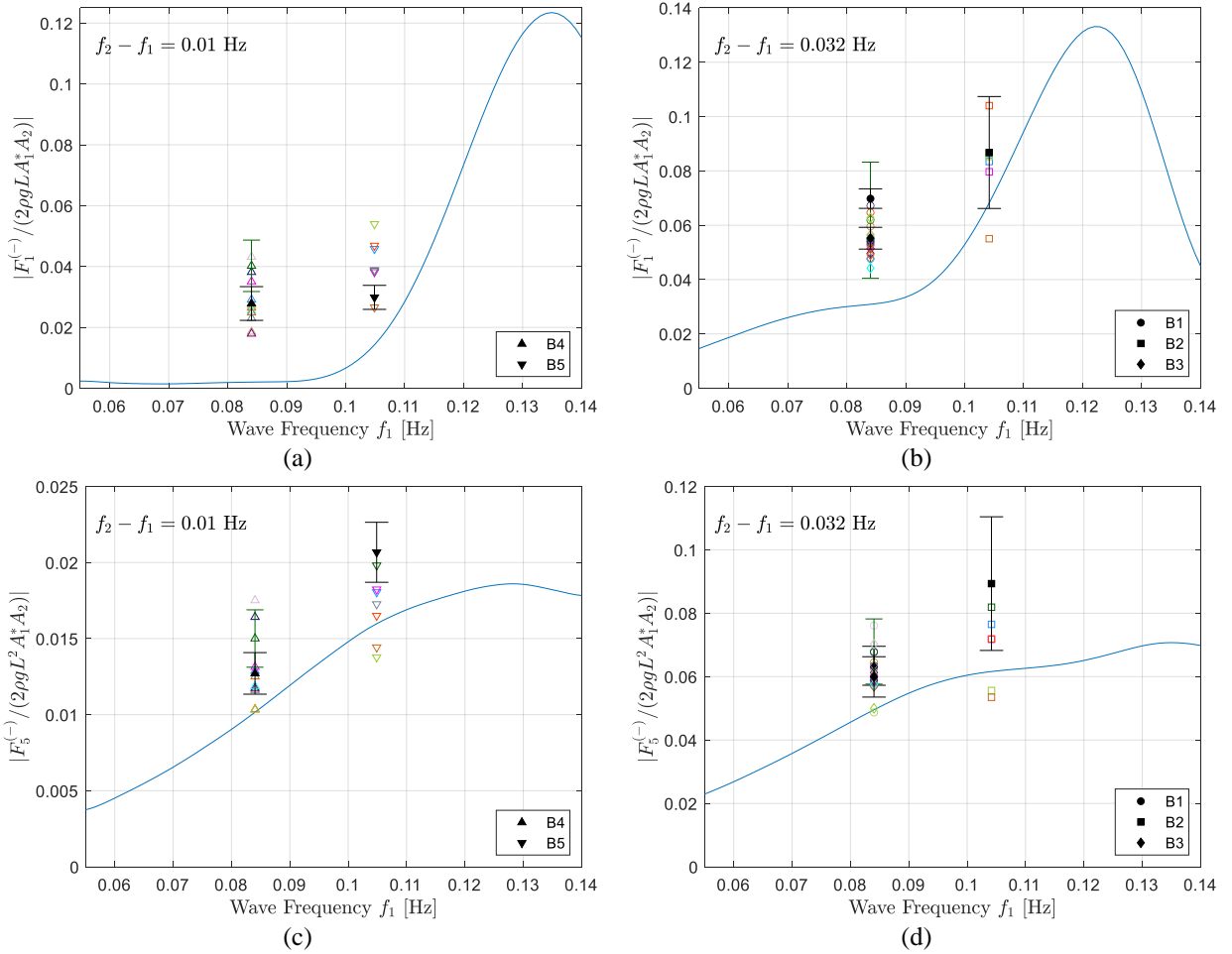


**Figure 17.** Comparison of the difference-frequency surge force (a,b) and pitch moment (c,d) among CFD

solutions, experimental measurements, and potential-flow QTFs. The difference frequency is either near the surge resonance frequency (a,c) or the pitch resonance frequency (b,d). The continuous lines are the potential-flow QTFs. The hollow symbols are CFD solutions, whereas the filled symbols are the experimental measurements. The different symbol shapes correspond to different bichromatic wave cases, and the different colors correspond to different CFD participants or the experiment (see figures in Section 7). The uncertainty bars with wider caps are for the experiment, and the ones with narrower caps, when present, are for the NREL CFD solutions.

## 9. Conclusions

This paper presented the validation of a set of CFD simulations of a fixed FOWT semisubmersible in bichromatic incident waves against the measurements from a new model-scale experimental campaign. Both the CFD simulations and the experimental campaign were performed as part of the OC6 Phase Ib project investigating the underprediction of the nonlinear, low-frequency wave excitation and the motion response of semisubmersible FOWTs by mid-fidelity engineering-level tools. The difference frequencies of the selected bichromatic-wave conditions were chosen to be close to either the surge or the pitch resonance frequencies of the structure in a floating condition, which fell below the typical wave-frequency range; therefore, special attention was paid to the nonlinear difference-frequency wave excitation during validation. We would like to validate the CFD predictions of the normalized amplitudes of the nonlinear surge force and pitch moment at the difference frequency. The normalized wave excitation at the wave frequencies were also included for completeness.

The validation is overall successful for most nonlinear, difference-frequency wave excitations with either overlapping experimental and CFD uncertainty bands and/or with multiple sets of CFD predictions falling within the experimental uncertainty ranges. Key observations from the validation study are summarized as follows:

- Compared to at the lower surge resonance frequency, the CFD simulations produce more consistent predictions at the pitch resonance frequency for both the surge force and the pitch moment. The agreement with the experimental measurements is also better in general.
- The agreement among CFD predictions and between the CFD and experimental results is generally better with lower wave heights, likely because of the reduced viscous drag contribution, which tends to be challenging to capture accurately with numerical simulations because of the mesh resolution required.
- At the surge resonance frequency, the CFD solutions show more scatter, especially with the difference-frequency surge force. The increased scatter is partially a consequence of the lower magnitudes of the nonlinear wave excitation, but it also relates to the increased contribution from viscous drag, relative to second-order wave diffraction.
- Despite the scatter among CFD predictions at the surge resonance frequency, the experiment still demonstrates a level of agreement with the CFD simulations in the difference-frequency surge force and

pitch moment, with the experimental measurements falling approximately in the center of the ranges spanned by all the CFD results.

- The experiment and the CFD simulations are generally in good agreement in terms of the wave excitations at the two primary frequencies of the bichromatic waves.

The experimental and CFD results were also compared to the difference-frequency wave-load QTFs from second-order potential-flow theory, which were found to severely underpredict the difference-frequency surge force and less severely but still appreciably underpredict the pitch moment. Some key observations from the comparison of the global wave excitation on the entire structure are summarized as follows:

- The potential-flow QTF severely underpredicts the difference-frequency surge force by approximately a factor of 2 near the pitch resonance frequency and by at least an order of magnitude near the surge resonance frequency.
- The underprediction of the surge force is most likely caused by the additional viscous drag excitation on the structure not considered in the potential-flow theory. The viscous drag excitation appears to be the dominant contributor to the difference-frequency surge force at the surge resonance frequency.
- The underprediction of the difference-frequency pitch moment by the potential-flow QTF is not as significant. The underprediction is typically between 20% and 40%, depending on the wave conditions.

Compared to prior investigations of the nonlinear, low-frequency hydrodynamics with bichromatic waves, a special feature of the present experimental campaign is the use of a simplified floater geometry to allow the wave loads on each column of the semisubmersible to be measured separately, which enables a better understanding of the effects of hydrodynamic interaction among the three columns of the floater on the nonlinear difference-frequency loads. In the current paper, it facilitates a more detailed validation of the CFD solutions involving the comparison of the wave loads on each column separately. For a formal validation, the present investigation also includes uncertainty analyses for all quantities of interest for both the experiment and selected CFD simulations. To our knowledge, a large-scale collaborative validation effort of high-fidelity CFD simulations focusing on the nonlinear difference-frequency wave loads on a floating wind semisubmersible with uncertainty estimates is not readily found in the literature despite its engineering significance. By comparing with potential-flow predictions, the present study also confirms some of the persistent underprediction of nonlinear wave loads observed in prior investigations.

1  
2  
3  
4 Despite the overall successful validation, the relatively large uncertainties of the CFD solutions for some load  
5 cases limit the confidence in the conclusion. In the future, efforts should be made to further refine the CFD setup to  
6 reduce uncertainty and variability in the predictions. Further, the present investigation considers only a fixed  
7 structure and wave diffraction loads. For a full understanding of the low-frequency hydrodynamics, future validation  
8 effort should also consider a moored floating structure.  
9

10  
11 Overall, this validation effort shows that CFD simulations can provide meaningful predictions of the nonlinear,  
12 difference-frequency wave excitation in surge and pitch that are mostly consistent with experimental measurements;  
13 therefore, CFD simulations can be used as references for tuning mid-fidelity engineering tools. Further, we hope that  
14 the wealth of data that can be extracted from CFD simulations will provide us with a better understanding of the  
15 underprediction by mid-fidelity engineering-level tools of the nonlinear low-frequency wave excitation and  
16 structural response and lead to improvements to the model formulation and modeling practices of such tools.  
17  
18  
19  
20  
21  
22  
23  
24  
25  
26

## 27 **Acknowledgments**

28  
29 This work was authored in part by the National Renewable Energy Laboratory, operated by Alliance for  
30 Sustainable Energy, LLC, for the U.S. Department of Energy (DOE) under Contract No. DE-AC36-08GO28308.  
31 Funding provided by the U.S. Department of Energy Office of Energy Efficiency and Renewable Energy Wind  
32 Energy Technologies Office. The views expressed in the article do not necessarily represent the views of the DOE or  
33 the U.S. Government. The U.S. Government retains and the publisher, by accepting the article for publication,  
34 acknowledges that the U.S. Government retains a nonexclusive, paid-up, irrevocable, worldwide license to publish  
35 or reproduce the published form of this work, or allow others to do so, for U.S. Government purposes.  
36  
37  
38  
39  
40  
41  
42  
43  
44

45 A portion of the research was performed using computational resources sponsored by the Department of  
46 Energy's Office of Energy Efficiency and Renewable Energy and located at the National Renewable Energy  
47 Laboratory.  
48  
49  
50

51 The University of Plymouth team would like to acknowledge the ongoing support of the Engineering and  
52 Physical Sciences Research Council (EPSRC) via project EP/T004177/1.  
53  
54

55 MARIN would like to acknowledge that their contribution is partly funded by the Dutch Ministry of Economic  
56 Affairs.  
57  
58  
59  
60  
61  
62  
63  
64  
65



## References

- ANSYS Inc., 2018. ANSYS Fluent 19.2 User Guide.
- ASME, 2013. Test uncertainty, performance test codes. ASME PTC 19.1-2013.
- Azcona, J., Bouchotrouch, F., Vittori, F., 2019. Low- frequency dynamics of a floating wind turbine in wave tank-scaled experiments with SiL hybrid method. *Wind Energy* 22, 1402-1413. <https://doi.org/10.1002/we.2377>.
- Bayati, I., Jonkman, J., Robertson, A., Platt, A., 2014. The effects of second-order hydrodynamics on a semisubmersible floating offshore wind turbine. *J. Phys.: Conf. Ser.* 524(1), 012094. <https://doi.org/10.1088/1742-6596/524/1/012094>.
- Betta, G., Liguori, C., Pietrosanto, A., 2000. Propagation of uncertainty in a discrete Fourier transform algorithm. *Measurement* 27(4), 231-239. [https://doi.org/10.1016/S0263-2241\(99\)00068-8](https://doi.org/10.1016/S0263-2241(99)00068-8).
- Boccotti, P. 1996. Inertial wave loads on horizontal cylinders: A field experiment. *Ocean Eng.* 23(7), 629-648. [https://doi.org/10.1016/0029-8018\(96\)00003-0](https://doi.org/10.1016/0029-8018(96)00003-0).
- Burmester, S., Vaz, G., el Moctar, O., Gueydon, S., Koop, A., Wang, Y., Chen, H.C., 2020a. High-fidelity modelling of floating offshore wind turbine platforms. Proceedings of the ASME 2020 39th International Conference on Ocean, Offshore and Arctic Engineering, V009T09A068. Virtual, Online. <https://doi.org/10.1115/OMAE2020-18913>.
- Burmester, S., Vaz, G., Gueydon, S., el Moctar, O., 2020b. Investigation of a semi-submersible floating wind turbine in surge decay using CFD. *Ship Tech. Res.* 67(1), 2-14. <https://doi.org/10.1080/09377255.2018.1555987>.
- Canet, H., Bortolotti, P., and Bottasso, C.L., 2021. On the scaling of wind turbine rotors. *Wind Energy Sci.*, 6, 601-626. <https://doi.org/10.5194/wes-6-601-2021>.
- Clément, C., Bozonnet, P., Vinay, G., Borràs Nadal, A., Pagnier, P., Réveillon, J., 2020. Numerical wave tank including a fixed vertical cylinder subjected to waves, towards the investigation of floating offshore wind turbine hydrodynamics. Proceedings of ASME 2020 39th International Conference on Ocean, Offshore and Arctic Engineering, V06AT06A015. Virtual, Online. <https://doi.org/10.1115/OMAE2020-18797>.
- Devolder, B., Troch, P., Rauwoens, P., 2018. Performance of a buoyancy-modified  $k-\omega$  and  $k-\omega$  SST turbulence model for simulating wave breaking under regular waves using OpenFOAM®. *Costal Eng.* 138, 49-65. <https://doi.org/10.1016/j.coastaleng.2018.04.011>.
- do Carmo, L.H.S., de Mello, P.C., Malta, E.B., Franzini, G.R., Simos, A.N., Gonçalves, R.T., Suzuki, H., 2020. Analysis of a FOWT model in bichromatic waves: An investigation on the effect of combined wave-frequency and slow motions on the calibration of drag and inertial force coefficients. Proceedings of the ASME 2020 39th International Conference on Ocean, Offshore and Arctic Engineering, V009T09A047. Virtual, Online. <https://doi.org/10.1115/OMAE2020-18239>.
- Eça, L., 2006. On the influence of the iterative error in the numerical uncertainty of ship viscous flow calculations. Proceedings of the 26th Symposium on Naval Hydrodynamics. Rome, Italy.
- Eça, L., Hoekstra, M., 2009. Evaluation of numerical error estimation based on grid refinement studies with the method of the manufactured solutions. *Comput. Fluids* 38, 1580-1591. <https://doi.org/10.1016/j.compfluid.2009.01.003>.
- Eça, L., Hoekstra, M., 2014. A procedure for the estimation of the numerical uncertainty of CFD calculations based on grid refinement studies. *J. Comput. Phys.* 262, 104-130. <https://doi.org/10.1016/j.jcp.2014.01.006>.
- Eça, L., Vaz, G., Hoekstra, M., 2018. On the role of iterative errors in unsteady flow simulations. Proceedings of the 21st Numerical Towing Tank Symposium (NuTTS 2018). Cortona, Italy.
- Eça, L., Vaz, G., Toxopeus, S.L., Hoekstra, M., 2019. Numerical errors in unsteady flow simulations. *J. Verif. Valid. Uncert.* 4(2), 021001. <https://doi.org/10.1115/1.4043975>.
- Farrance, I., Frenkel, R., 2012. Uncertainty of measurement: A review of the rules for calculating uncertainty components through functional relationships. *Clin. Biochem. Rev.* 33(2), 49-75.

- 1
- 2
- 3
- 4 Ferreira González, D., Götsche, U., Netzband, S., Abdel-Maksoud, M., 2021. Advances on simulations of wave-
- 5 body interactions under consideration of the nonlinear free water surface. *Ship Tech. Res.* 68(1), 27-40.
- 6 <https://doi.org/10.1080/09377255.2020.1836551>.
- 7
- 8 Fowler, M., 2021. 1/50-scale DeepCwind Semi-Submersible Component Wave Testing. University of Maine,
- 9 Advanced Structures and Composites Center. Orono: University of Maine.
- 10
- 11 Hirt, C.W., Nichols, B.D., 1981. Volume of Fluid (VOF) method for the dynamics of free boundaries. *J. Comput.*
- 12 *Phys.* 39(1), 201-225. [https://doi.org/10.1016/0021-9991\(81\)90145-5](https://doi.org/10.1016/0021-9991(81)90145-5).
- 13
- 14 Jacobsen, N.G., Fuhrman, D.R., Fredsøe, J., 2012. A wave generation toolbox for the open-source CFD library:
- 15 OpenFoam®. *Int. J. Numer. Methods Fluids* 70(9), 1073-1088. <https://doi.org/10.1002/flid.2726>.
- 16
- 17 Jonkman, J.M., 2013. The new modularization framework for the FAST Wind Turbine CAE Tool. Proceedings of
- 18 the 51st AIAA Aerospace Sciences Meeting including the New Horizons Forum and Aerospace Exposition.
- 19 Grapevine, TX, USA. <https://doi.org/10.2514/6.2013-202>.
- 20
- 21 Klaij, C.M., Hoekstra, M., Vaz, G., 2018. Design, analysis and verification of a volume-of-fluid model with
- 22 interface-capturing scheme. *Comput. Fluids* 170, 324-340. <https://doi.org/10.1016/j.compfluid.2018.05.016>.
- 23
- 24 Larsen, B.E., Fuhrman, D.R., 2018. On the over-production of turbulence beneath surface waves in Reynolds-
- 25 averaged Navier-Stokes models. *J. Fluid Mech.* 853, pp. 419-460. <https://doi.org/10.1017/jfm.2018.577>.
- 26
- 27 Lee, C.-H., 1995. WAMIT Theory Manual. Massachusetts Institute of Technology, Cambridge, MA, USA.
- 28 <http://wamit.com/Publications/tmanual.pdf> (accessed 21 May 2021).
- 29
- 30 Leimeister, M., Kolios, A., Collu, M., 2018. Critical review of floating support structures for offshore wind farm
- 31 deployment. *J. Phys.: Conf. Ser.* 1104, 012007. <https://doi.org/10.1088/1742-6596/1104/1/012007>.
- 32
- 33 Lopez-Pavon, C., Watai, R.A., Ruggeri, F., Simos, A.N., Souto-Iglesias, A., 2015. Influence of wave induced
- 34 second-order forces in semisubmersible FOWT mooring design. *J. Offshore Mech. Arct. Eng.* 137(3),
- 35 031602. <https://doi.org/10.1115/1.4030241>.
- 36
- 37 Lykke Andersen, T., Eldrup, M.R., Clavero, M., 2019. Separation of long-crested nonlinear bichromatic waves into
- 38 incident and reflected components. *J. Mar. Sci. Eng.* 7, 39. <https://doi.org/10.3390/jmse7020039>.
- 39
- 40 Maienza, C., Avossa, A.M., Ricciardelli, F., Coiro, D., Troise, G., Georgakis, C.T., 2020. A life cycle cost model for
- 41 floating offshore wind farms. *Appl. Energy* 266, 114716. <https://doi.org/10.1016/j.apenergy.2020.114716>.
- 42
- 43 Martin, H.R., Kimball, R.W., Viselli, A.M., Goupee, A.J., 2014. Methodology for wind/wave basin testing of
- 44 floating offshore wind turbines. *J. Offshore Mech. Arct. Eng.* 136, 020905.
- 45 <https://doi.org/10.1115/1.4025030>.
- 46
- 47 Méhauté, B.L., 1976. Similitude in coastal engineering. *J. Waterw. Harb. Coast. Eng. Div.* 102(3), 317-335.
- 48 <https://doi.org/10.1061/AWHCAR.0000332>.
- 49
- 50 Musial, W., Butterfield, S., 2004. Future for offshore wind energy in the United States. Proceedings of EnergyOcean
- 51 2004. Palm Beach, Florida.
- 52
- 53 Park, C., Kim, G.D., Yim, G.-T., Park, Y., Moon, I., 2020. A validation study of the model test method for propeller
- 54 cavitation noise prediction. *Ocean Eng.* 213, 107655. <https://doi.org/10.1016/j.oceaneng.2020.107655>.
- 55
- 56 Pegalajar-Jurado, A., Bredmose, H., 2016. Reproduction of slow-drift motions of a floating wind turbine using
- 57 second-order hydrodynamics and Operational Modal Analysis. *Mar. Struct.* 66, 178-196.
- 58 <https://doi.org/10.1016/j.marstruc.2019.02.008>.
- 59
- 60 ReFRESCO, 2020. [www.refresco.org](http://www.refresco.org) (accessed 21 May 2021).
- 61
- 62 Robertson, A.N., 2021. OC6 Phase Ib: Additional data focused on Phase 1 geared toward CFD validation.
- 63 <https://a2e.energy.gov/data/oc6/oc6.phase1b> (accessed 21 May 2021).
- 64
- 65 Robertson, A.N., Bachynski, E., Gueydon, S., Wendt, F., Schünemann, P., 2020a. Total experimental uncertainty in
- hydrodynamic testing of a semisubmersible wind turbine, considering numerical propagation of systematic
- uncertainty. *Ocean Eng.* 195, 106605. <https://doi.org/10.1016/j.oceaneng.2019.106605>.

- 1
- 2
- 3
- 4 Robertson, A.N., Bachynski, E.E., Gueydon, S., Wendt, F., Schünemann, P., Jonkman, J., 2018. Assessment of
- 5 experimental uncertainty for a floating wind semisubmersible under hydrodynamic loading. Proceedings of
- 6 the ASME 2018 37th International Conference on Ocean, Offshore and Arctic Engineering, V010T09A076.
- 7 Madrid, Spain. <https://doi.org/10.1115/OMAE2018-77703>.
- 8
- 9 Robertson, A.N., Gueydon, S., Bachynski, E., Wang, L., Jonkman, J., Alarcón, D., Amet, E., Beardsell, A., Bonnet,
- 10 P., Boudet, B., et al., 2020b. OC6 Phase I: Investigating the underprediction of low-frequency hydrodynamic
- 11 loads and responses of a floating wind turbine. J. Phys.: Conf. Ser. 1618(3), 032033.
- 12 <https://doi.org/10.1088/1742-6596/1618/3/032033>.
- 13
- 14 Robertson, A.N., Wendt, F., Jonkman, J.M., Popko, W., Dagher, H., Gueydon, S., Qvist, J., Vittori, F., Azcona, J.,
- 15 Uzunoglu, E., et al., 2017. OC5 Project Phase II: Validation of global loads of the DeepCwind floating
- 16 semisubmersible wind turbine. Energy Procedia 137, 38-57. <https://doi.org/10.1016/j.egypro.2017.10.333>.
- 17
- 18 Sharma, J.N., Dean, R.G., 1982. Second-order directional seas and associated wave forces. Soc. Pet. Eng. J. 21(1),
- 19 129-140. <https://doi.org/10.2118/8584-PA>.
- 20
- 21 Siemens PLM Software, 2018. Simcenter STAR-CCM+ User Guide, Version 13.06.012.
- 22
- 23 Simos, A.N., Ruggeri, F., Watai, R.A., Souto-Iglesias, A., Lopez-Pavon, C., 2018. Slow-drift of a floating wind
- 24 turbine: An assessment of frequency-domain methods based on model tests. Renew. Energy 116, 133-154.
- 25 <https://doi.org/10.1016/j.renene.2017.09.059>.
- 26
- 27 Simos, A.N., Sparano, J.V., Aranha, J.A.P., Matos, V.L.F., 2008. 2nd order hydrodynamic effects on resonant
- 28 heave, pitch and roll motions of a large-volume semi-submersible platform. Proceedings of the ASME 27th
- 29 International Conference on Offshore Mechanics and Arctic Engineering, pp. 229-237. Estoril, Portugal.
- 30 <https://doi.org/10.1115/OMAE2008-57430>.
- 31
- 32 Tom, N., Robertson, A., Jonkman, J., Wendt, F., Böhm, M., 2019. Bichromatic wave selection for validation of the
- 33 difference-frequency transfer function for the OC6 validation campaign. Proceedings of the 2nd
- 34 International Offshore Wind Technical Conference, V001T01A022. St. Julian's, Malta.
- 35 <https://doi.org/10.1115/IOWTC2019-7572>.
- 36
- 37 Ueno, M., Tsukada, Y., 2015. Rudder effectiveness and speed correction for scale model ship testing. Ocean Eng.
- 38 109, 495-506. <https://doi.org/10.1016/j.oceaneng.2015.09.041>.
- 39
- 40 Waals, O.J., 2009. On the application of advanced wave analysis in shallow water model testing (wave splitting).
- 41 Proceedings of the ASME 28th International Conference on Ocean, Offshore and Arctic Engineering, pp.
- 42 415-423. Honolulu, Hawaii, USA. <https://doi.org/10.1115/OMAE2009-79413>.
- 43
- 44 WAMIT, Inc., 2011. WAMIT User Manual Version 6.1, 6.1PC, 6.1S, 6.1S-PC. Chestnut Hill, MA.
- 45
- 46 Wang, L., Robertson, A., Jonkman, J., Yu, Y.-H., 2021a. Uncertainty assessment of CFD investigation of the
- 47 nonlinear difference-frequency wave loads on a semisubmersible FOWT platform. Sustainability 13(1), 64.
- 48 <https://doi.org/10.3390/su13010064>.
- 49
- 50 Wang, L., Robertson, A., Jonkman, J., Yu, Y.-H., Koop, A., Borràs Nadal, A., Li, H., Shi, W., Pinguet, R., Zhou, Y.,
- 51 Xiao, Q., Kumar, R., Sarlak, H., 2021b. Investigation of nonlinear difference-frequency wave excitation on a
- 52 semisubmersible offshore-wind platform with bichromatic-wave CFD simulations. Proceedings of the
- 53 ASME 2021 3rd International Offshore Wind Technical Conference, V001T01A009. Virtual, Online.
- 54 <https://doi.org/10.1115/IOWTC2021-3537>.
- 55
- 56 Wang, W., Wu, M., Palm, J., Eskilsson, C., 2018. Estimation of numerical uncertainty in computational fluid
- 57 dynamics simulations of a passively controlled wave energy converter. Proc. I. Mech. Eng. Part M.: J. Eng.
- 58 Marit. Environ. 232(1), 71-84. <https://doi.org/10.1177/1475090217726884>.
- 59
- 60 Wang, Y., Chen, H.C., Vaz, G., Burmester, S., 2019. CFD simulation of semi-submersible floating offshore wind
- 61 turbine under pitch decay motion. Proceedings of the ASME 2019 2nd International Offshore Wind
- 62 Technical Conference, V001T01A002. St. Julian's, Malta. <https://doi.org/10.1115/IOWTC2019-7515>.
- 63
- 64 Wang, Y., Chen, H.C., Vaz, G., Mewes, S., 2021c. Verification study of CFD simulation of semi-submersible
- 65 floating offshore wind turbine under regular waves. Proceedings of the ASME 2021 3rd International

Offshore Wind Technical Conference, V001T01A010. Virtual, Online.  
<https://doi.org/10.1115/IOWTC2021-3558>.

Weller, H.G., Tabor, G., Jasak, H., Fureby, C., 1998. A tensorial approach to computational continuum mechanics using object-oriented techniques. *Comput. Phys.* 12(6), 620-631. <https://doi.org/10.1063/1.168744>.

Williamson, C.H.K., 1984. Sinusoidal flow relative to circular cylinders, *J. Fluid Mech.* 155, 141-174.  
<https://doi.org/10.1017/S0022112085001756>.

Windt, C., Davidson, J., Ringwood, J.V., 2021. Investigation of turbulence modeling for point-absorber-type wave energy converters. *Energies* 14(1), 26. <https://doi.org/10.3390/en14010026>.

Yamini, O.A., Kavianpour, M.R., Hooman Mousavi, S., 2018. Wave run-up and rundown on ACB mats under granular and geotextile filters' condition. *Mar. Georesources Geotechnol.* 36(8), 895-906.  
<https://doi.org/10.1080/1064119X.2017.1397068>.

## Glossary

$A_b^f$	Amplitude of the forward bound wave at the difference frequency, $f_d$
$A_d$	Total wave amplitude at frequency $f_d$
$A_d^b$	Amplitude of the backward free wave at frequency $f_d$
$A_d^f$	Amplitude of the forward free wave at frequency $f_d$
$A_m$	Total wave amplitude at one of the primary wave frequencies, $f_m$
$A_m^b$	Amplitude of the backward wave at frequency $f_m$
$A_m^f$	Amplitude of the forward wave at frequency $f_m$
$F_j^{(-)}$	Amplitude of the wave load in mode $j$ at the difference frequency, $f_d$
$\tilde{F}_j^{(-)}$	$F_j^{(-)}$ with correction for wave reflection and contamination
$F_{j,m}$	Amplitude of the wave load in mode $j$ at one of the primary wave frequencies, $f_m$
$\tilde{F}_{j,m}$	$F_{j,m}$ with correction for wave reflection
$f_d$	Difference frequency
$f_m$	Primary wave frequencies with $m = 1,2$
$g$	Gravitational acceleration
$k_b$	Wave number of the difference-frequency bound wave
$k_d$	Wave number of the difference-frequency free wave
$k_m$	Wave numbers of the primary wave components with $m = 1,2$
$L$	Center-to-center distance between columns of the semisubmersible
$T_m$	Periods of the primary wave components with $m = 1,2$
$T_R$	Repeat periods of the bichromatic waves
$X_j^{(-)}$	Normalized amplitude of the wave load in mode $j$ at the difference frequency
$\tilde{X}_j^{(-)}$	$X_j^{(-)}$ with correction for wave reflection and contamination
$X_{j,m}$	Normalized amplitude of the wave load in mode $j$ at the primary wave frequency, $f_m$
$\tilde{X}_{j,m}$	$X_{j,m}$ with correction for wave reflection
$U_w$	Uncertainties in $X_j^{(-)}$ and $X_{j,m}$ from wave reflection and contamination
$\rho$	Density of water

## Appendix

**Table A.1.** CFD software and numerical schemes adopted by OC6 participants.

Participant	CFD Software	Temporal Discretization		Spatial Discretization			Pressure-Velocity Coupling			
		Temporal Discretization Scheme	Time Step	Momentum Convection	Other	Volume Fraction	Algo.	No. of Press. Corr.	Res. Tol.	Max Outer Iter.
CENER National Renewable Energy Centre	OpenFOAM ver. 1812 waves2Foam	1 <sup>st</sup> order implicit (backward Euler)	Adaptive based on Co	Gauss linear upwind	Gauss linear	MULES	PISO	3	N/A	N/A
DTU Tech. Univ. Denmark	OpenFOAM ver. 1812 waves2Foam	2 <sup>nd</sup> order implicit blended Crank- Nicolson and Euler	$T_2/1030$	Gauss limitedLinearV	Gauss linear	MULES	PISO	Wave B1: 10 All Other: 3	N/A	N/A
DUT Dalian Univ. Tech.	STAR-CCM+ ver. 14.06.013	2 <sup>nd</sup> order implicit	$T_2/1030$	2 <sup>nd</sup> order upwind for convection Hybrid Gauss-LSQ for gradient		HRIC	SIMPLE	N/A	None	20
IFPEN IFP Energies nouvelles	OpenFOAM ver. 1812 waves2Foam	2 <sup>nd</sup> order implicit blended Crank- Nicolson and Euler	$T_2/1030$	Gauss linear	Self-filtered central differencing (SFCD)	MULES	PISO	3	N/A	N/A
MARIN Maritime Research Inst. Netherlands	ReFresco ver. 2.7	2 <sup>nd</sup> order implicit	$T_2/1030$	2 <sup>nd</sup> order harmonic TVD scheme of Van Leer		ReFRICS (Klaaij et al., 2018)	SIMPLE	N/A	$10^{-6}$	50
NREL National Renewable Energy Laboratory	STAR-CCM+ ver. 13.06.012	2 <sup>nd</sup> order implicit	$T_2/1030$	2 <sup>nd</sup> order upwind for convection Hybrid Gauss-LSQ for gradient		HRIC	SIMPLE	N/A	None	20
NTNU Norwegian Univ. of Sci. & Tech.	OpenFOAM ver. 1712 waves2Foam	1 <sup>st</sup> order implicit (backward Euler)	0.001414	Gauss limitedLinearV	Gauss linear	MULES	PISO	3	N/A	N/A
PPI Principle Power, Inc.	OpenFOAM ver. 1812 waves2Foam	2 <sup>nd</sup> order implicit blended Crank- Nicolson and Euler	$T_2/1030$	Gauss upwind	Gauss linear	MULES	PISO	3	Pressure $10^{-6}$	N/A
UOP Univ. Plymouth	OpenFOAM ver. 1906 waves2Foam	2 <sup>nd</sup> order implicit blended Crank- Nicolson and Euler	$T_2/1030$	Gauss linear		MUSCL	PIMPLE	3	$10^{-7}$	3
UOS Univ. Strathclyde	OpenFOAM ver. 4.x waves2Foam	1 <sup>st</sup> order implicit (backward Euler)	$T_2/2438$	Gauss limitedLinearV	Gauss linear	MULES	PIMPLE	2	$10^{-8}$	10
UOU Univ. Ulsan	ANSYS Fluent ver. 19.2	2 <sup>nd</sup> order implicit	$T_2/862$	2 <sup>nd</sup> order upwind for convection Least squares for gradient		CICSAM	SIMPLE	N/A	None	35

Table A.2. Other numerical settings of OC6 participants. All dimensions are at model scale.

Participant	Domain		Floater Boundary Condition	Wave Forcing/Relaxation/Damping Zones			Reference Incident Wave Field	Turbulence Model
	Domain Width <sup>1</sup>	Half Domain		Length of Upstream Wave Forcing Zone	Downstream Wave Zone			
					Type	Length		
CENER National Renewable Energy Centre	4 m	No	No slip	6 m	Relaxation	8.89 m	2 <sup>nd</sup> order bichromatic	None
DTU Tech. Univ. Denmark	4 m	No	No slip	$1.5\lambda_1$	Relaxation	$2\lambda_1$	2 <sup>nd</sup> order bichromatic	None
DUT Dalian Univ. Tech.	9 m	Yes	No slip	8.02 m	Relaxation	8.02 m	Linear superposition	None
IFPEN IFP Energies nouvelles	9 m	No	Free slip	2.37 m	Relaxation	18.68 m	Linear superposition	None
MARIN Maritime Research Inst. Netherlands	4 m	Yes	No slip	4.42 m	Relaxation	4.42 m	Linear superposition	None
NREL National Renewable Energy Laboratory	9 m	Yes	No slip	None	Damping	8.84 m	Linear superposition	None
NTNU Norwegian Univ. of Sci. & Tech.	9 m	No	No slip	4.42 m	Relaxation	17.71 m	2 <sup>nd</sup> order bichromatic	None
PPI Principle Power, Inc.	4 m	No	No slip	6.63 m	Relaxation	8.84 m	2 <sup>nd</sup> order bichromatic	None
UOP Univ. Plymouth	4 m	No	Free slip	6.593 m	Relaxation	9.51 m	2 <sup>nd</sup> order bichromatic	None
UOS Univ. Strathclyde	4 m	No	No slip	4.42 m	Relaxation	8.84 m	Linear superposition	None
UOU Univ. Ulsan	9 m	Yes	No slip	None	Damping	$2\lambda_1$	Linear superposition	None

1. If a half domain is used with port-starboard symmetry, the actual width of the numerical domain is a half of this value. A width of 9 m matches the physical wave basin exactly. The length of the domain, 39 m, and the distance from the floater to the wave maker, 8.84 m, are consistent across all participants.